PHYSICAL REVIEW D **91,** 103533 (2015)

Probing WIMP particle physics and astrophysics with direct detection and neutrino telescope data

Bradley J. Kavanagh,[1,2,*] Mattia Fornasa,[1,3,†] and Anne M. Green[1,‡]

[1]*School of Physics & Astronomy, University of Nottingham, University Park,*
Nottingham NG7 2RD, United Kingdom
[2]*Institut de physique théorique, Université Paris Saclay, CNRS, CEA, F-91191 Gif-sur-Yvette, France*
[3]*GRAPPA Institute, University of Amsterdam, Science Park 904, 1098 XH Amsterdam, Netherlands*

(Received 17 November 2014; published 26 May 2015)

With positive signals from multiple direct detection experiments, it will, in principle, be possible to measure the mass and cross sections of weakly interacting massive particle (WIMP) dark matter. Recent work has shown that, with a polynomial parametrization of the WIMP speed distribution, it is possible to make an unbiased measurement of the WIMP mass, without making any astrophysical assumptions. However, direct detection experiments are not sensitive to low-speed WIMPs and, therefore, any model-independent approach will lead to a bias in the cross section. This problem can be solved with the addition of measurements of the flux of neutrinos from the Sun. This is because the flux of neutrinos produced from the annihilation of WIMPs which have been gravitationally captured in the Sun is sensitive to low-speed WIMPs. Using mock data from next-generation direct detection experiments and from the IceCube neutrino telescope, we show that the complementary information from IceCube on low-speed WIMPs breaks the degeneracy between the cross section and the speed distribution. This allows unbiased determinations of the WIMP mass and spin-independent and spin-dependent cross sections to be made, and the speed distribution to be reconstructed. We use two parametrizations of the speed distribution: binned and polynomial. While the polynomial parametrization can encompass a wider range of speed distributions, this leads to larger uncertainties in the particle physics parameters.

DOI: 10.1103/PhysRevD.91.103533 PACS numbers: 95.35.+d, 98.62.Gq, 14.80.-j, 07.05.Kf

I. INTRODUCTION

Experiments aiming at detecting dark matter (DM) *directly* rely on measuring the signatures left by DM particles when they interact with the nuclei of a detector [1,2]. This technique was devised to search for a specific class of DM candidates: weakly interacting massive particles (WIMPs) [3]. WIMPs characteristically have a mass of the order of GeV to TeV, and their elastic scatterings off target nuclei induce recoils with energy on the order of keV.

The number and energies of the recoil events can, in principle, be used to infer the properties of the DM particle, e.g. its mass and scattering cross sections. However, with a single experiment, this requires knowledge of the local WIMP velocity distribution, $f(\mathbf{v})$ (e.g. Ref. [4]). Data analyses usually use the so-called standard halo model (SHM), where the velocity distribution is assumed to have the following simple form (in the Galactic rest frame):

$$f_{\mathrm{Gal}}(\mathbf{v}) = \frac{1}{(2\pi\sigma_v^2)^{3/2}} \exp\left(-\frac{\mathbf{v}^2}{2\sigma_v^2}\right). \tag{1}$$

This corresponds to an isothermal, spherical DM halo with density profile $\rho(r) \propto r^{-2}$, in equilibrium, in which case the dispersion σ_v is related to the local circular speed $v_c \approx 220\ \mathrm{km\,s^{-1}}$ [5,6] by $\sigma_v = v_c/\sqrt{2}$. The SHM velocity distribution is usually truncated manually at the Galactic escape speed, which we take to be $v_{\mathrm{esc}} = 544\ \mathrm{km\,s^{-1}}$, consistent with the estimates from the RAVE survey [7,8].

Despite its simplicity and extensive use, it is unlikely that the SHM provides a good description of the DM velocity distribution. More realistic models have been proposed that allow for a triaxial DM halo [9], a more general density profile [10] and/or an anisotropic velocity distribution [11]. Furthermore, if the DM speed distribution is reconstructed self-consistently from the potential of the Milky Way [12,13] the resulting distribution deviates from the Maxwellian distribution of the SHM in Eq. (1).

Distribution functions extracted from N-body simulations also show deviations from the SHM [14–17]. In particular, DM substructures (e.g. streams) may lead to "spikes" in the speed distribution, while DM which has not yet completely phase-mixed (so-called "debris flows") gives broad features [18]. Simulations including baryonic physics suggest the possibility of a dark disk, produced by the DM tidally stripped from subhalos that are preferentially dragged into the stellar disk during the late stages of halo assembly [19,20]. The resulting dark disk corotates

---

[*] bradley.kavanagh@cea.fr
[†] fornasam@gmail.com
[‡] anne.green@nottingham.ac.uk

with approximately the same speed as the stellar disk, but with a smaller velocity dispersion $\sigma_v \sim 50\ \mathrm{km\,s^{-1}}$. This dark disk may contribute an additional 20%–100% of the density of the halo (depending on the merger history of the Milky Way), although more recent simulations [21] indicate a smaller density, ∼10%.

From the previous discussion it is clear that the velocity distribution is still a quite uncertain quantity, despite its fundamental importance in the interpretation of direct detection data [22–24]. Furthermore, probing the speed distribution would provide information on the structure and evolution of the Milky Way.

Various model-independent techniques have recently been introduced for analyzing direct detection data without rigid assumptions about the WIMP speed distribution, with the goal of obtaining unbiased constraints on the WIMP particle properties, e.g. [4,25–29]. See Ref. [30] for a review. In particular, Refs. [4,28] suggested employing an empirical parametrization of the velocity distribution, and using data from multiple experiments to constrain its parameters along with the WIMP mass and cross section. Care must still be taken with the choice of parametrization in order to avoid a biased determination of the WIMP mass [4,31]. We found that particular functional forms for the *logarithm* of $f(\mathbf{v})$, for instance Legendre and Chebyshev polynomials, allow an unbiased reconstruction of the WIMP mass [30,32,33]. However, if only direct detection data are used, data analysis is inevitably hindered by the lack of sensitivity to low-speed WIMPs that produce recoil energies below the experimental energy thresholds. As experiments are blind to low-speed WIMPs, they can only detect some unknown fraction of the WIMPs. This then translates into a biased reconstruction of the scattering cross section.

Here we provide a solution to this problem using (simulated) future measurements from neutrino telescopes of the flux of neutrinos from the Sun. WIMPs scattering off the nucleons in the Sun can lose enough energy to get captured in its gravitational potential [34–39]. They accumulate there until their density is high enough to annihilate, producing (among other particles) neutrinos that can travel to us and be detected by neutrino telescopes, such as IceCube [40]. The expected number of neutrinos depends on the WIMP capture rate in the Sun, which is sensitive to the velocity distribution of WIMPs *below* a certain value.

A xenon-based direct detection experiment with $\mathcal{O}(\mathrm{keV})$ energy threshold is sensitive to WIMPs with speeds above $500\ \mathrm{km\,s^{-1}}$ for light WIMPs with mass of order a few GeV, or above tens of $\mathrm{km\,s^{-1}}$ for heavier WIMPs. On the other hand, the maximum solar capture speed (above which WIMPs are too fast to be captured) is larger than this for WIMP masses between 10 GeV and 1 TeV. Neutrino telescopes are, therefore, sensitive to the entire low-speed WIMP population which lies below the direct detection energy threshold. This indicates that combining direct detection and neutrino telescope data will allow us to probe the entire speed distribution and improve the accuracy of the constraints obtainable on both the WIMP mass and interaction cross section.

The complementarity of direct detection and neutrino telescope experiments has been studied previously in Ref. [41]. In that paper, astrophysical uncertainties were included by marginalizing over parameters of the SHM, and by comparing with the results obtained assuming speed distributions from N-body simulations. In the current work, we account for such uncertainties using two general parametrizations of $f(v)$ described above and investigate how well $f(v)$ can be reconstructed from data. Due to the degeneracy between the WIMP mass and speed distribution, such a general approach requires complementary information from several direct detection experiments, rather than a single experiment, as considered in Ref. [41].

In the following sections we estimate the sensitivity of this general approach by means of Bayesian inference. We choose a set of well-motivated benchmarks for the mass and cross sections of the WIMP, as well as for its speed distribution. For each of these benchmarks we simulate the data expected in next-generation direct detection experiments and in a neutrino telescope. These data are encoded in a likelihood function, with which we scan over a parameter space that includes both particle physics quantities (e.g. the WIMP mass and scattering cross sections) and astrophysical ones (e.g. the coefficients entering in our parametrization of the speed distribution). This technique allows us to estimate the precision with which future experiments will be able to reconstruct these parameters.

The paper is organized as follows. In Sec. II we summarize the formalism for the computation of recoil events in a direct detection experiment, as well as the expected signal in a neutrino telescope. In Sec. III we introduce the benchmark models considered and the parametrizations of the speed distribution. We also describe the sampling technique. In Sec. IV we present our results based on direct detection data only, while in Sec. V we also include the information from a neutrino telescope. Finally, we discuss our results in Sec. VII and summarize our main conclusions in Sec. VIII.

II. DARK MATTER EVENT RATE FORMALISM

A. Direct detection

The differential event rate per unit time and detector mass for nuclear recoils of energy E_R in a direct detection experiment is given by [42]

$$\frac{\mathrm{d}R}{\mathrm{d}E_R} = \frac{\rho_0}{m_\chi m_\mathrm{N}} \int_{v_\mathrm{min}}^{\infty} v f_1(v) \frac{\mathrm{d}\sigma}{\mathrm{d}E_\mathrm{R}} \mathrm{d}v. \tag{2}$$

The local DM mass density is denoted by ρ_0, the WIMP mass by m_χ and the target nuclear mass by m_N. The prefactor $\rho_0/(m_\chi m_\mathrm{N})$ is the number of WIMPs per unit volume multiplied by the number of target nuclei per unit detector mass. The integral in Eq. (2) is of the differential cross section weighted by the one-dimensional WIMP speed distribution $f_1(v)$ (see later).

The WIMP velocity distribution in the Earth's frame is related to that in the Galactic frame by a Galilean transformation: $f(\mathbf{v}) = f_\mathrm{Gal}(\mathbf{v} - \mathbf{v}_\mathrm{lag})$, where $\mathbf{v}_\mathrm{lag} \approx 230\ \mathrm{km\,s^{-1}}$ is the velocity of the Earth with respect to the Galactic rest frame [43,44]. This includes a contribution from the velocity of the Sun with respect to the Galactic frame as well as a contribution from the Earth's motion as it orbits the Sun. The dependence on the Earth's orbit implies that the velocity distribution will be time-varying, producing an annual modulation in the event rate [45]. However, this modulation is expected to be $\lesssim 10\%$ and we consider here only the time averaged event rate. The one-dimensional speed distribution is obtained by integrating over all directions in the Earth frame,

$$f_1(v) = \oint f_\mathrm{Gal}(\mathbf{v} - \mathbf{v}_\mathrm{lag}) v^2 \mathrm{d}\Omega_\mathbf{v} \equiv v^2 f(v). \tag{3}$$

The function $f(v)$ is the directionally averaged velocity distribution and is the quantity which we parametrize (and subsequently reconstruct) in order to account for astrophysical uncertainties.

The lower limit of the integral in Eq. (2) is the minimum WIMP speed that can excite a recoil of energy E_R,

$$v_\mathrm{min} = \sqrt{\frac{m_\mathrm{N} E_\mathrm{R}}{2\mu_{\chi\mathrm{N}}^2}}, \tag{4}$$

where $\mu_{\chi\mathrm{N}}$ is the reduced mass of the WIMP-nucleon system.

The differential cross section is typically divided into spin-dependent (SD) and spin-independent (SI) contributions:

$$\frac{\mathrm{d}\sigma}{\mathrm{d}E_\mathrm{R}} = \frac{\mathrm{d}\sigma_\mathrm{SD}}{\mathrm{d}E_\mathrm{R}} + \frac{\mathrm{d}\sigma_\mathrm{SI}}{\mathrm{d}E_\mathrm{R}}. \tag{5}$$

The SI contribution can be written as

$$\frac{\mathrm{d}\sigma_\mathrm{SI}}{\mathrm{d}E_\mathrm{R}} = \frac{m_\mathrm{N}\sigma_\mathrm{p}^\mathrm{SI}}{2\mu_{\chi\mathrm{p}}^2 v^2} A^2 F_\mathrm{SI}^2(E_\mathrm{R}), \tag{6}$$

where we have assumed that the coupling to protons and neutrons is equal ($f_\mathrm{p} = f_\mathrm{n}$). In this case, the SI contribution scales with the square of the mass number A of the target nucleus. The interaction strength is controlled by $\sigma_\mathrm{p}^\mathrm{SI}$, the WIMP-proton SI cross section, and by $\mu_{\chi\mathrm{p}} = m_\chi m_\mathrm{p}/(m_\chi + m_\mathrm{p})$, the reduced mass of the WIMP-proton system. The loss of coherence due to the finite size of the nucleus is captured in the form factor $F_\mathrm{SI}^2(E_\mathrm{R})$, which is obtained from the Fourier transform of the nucleon distribution in the nucleus. We take the form factor to have the Helm form [46]

$$F_\mathrm{SI}^2(E_\mathrm{R}) = \left[\frac{3j_1(qR_1)}{qR_1}\right]^2 \mathrm{e}^{-q^2 s^2}, \tag{7}$$

where $j_1(x)$ is a spherical Bessel function of the first kind and $q = \sqrt{2m_\mathrm{N}E_\mathrm{R}}$ is the momentum transfer. We use nuclear parameters from Ref. [47], based on fits to muon spectroscopy data [48]:

$$R_1 = \sqrt{c^2 + \frac{7}{3}\pi^2 a^2 - 5s^2}, \tag{8}$$

$$c = 1.23A^{1/3} - 0.60\ \mathrm{fm}, \tag{9}$$

$$a = 0.52\ \mathrm{fm}, \tag{10}$$

$$s = 0.9\ \mathrm{fm}. \tag{11}$$

Muon spectroscopy probes the *charge* distribution in the nucleus. However, detailed Hartree-Fock calculations indicate that the charge distribution can be used as a good proxy for the nucleon distribution (especially in the case $f_\mathrm{p} = f_\mathrm{n}$). It has been shown that using the approximate Helm form factor introduces an error of less than ~5% in the total event rate [49,50].

The standard expression for the SD contribution is

$$\frac{\mathrm{d}\sigma_\mathrm{SD}}{\mathrm{d}E_\mathrm{R}} = \frac{m_\mathrm{N}\sigma_\mathrm{p}^\mathrm{SD}}{2\mu_{\chi\mathrm{p}}^2 v^2} \frac{4(J+1)}{3J} \left(\langle S_\mathrm{p}\rangle + \frac{a_\mathrm{n}}{a_\mathrm{p}}\langle S_\mathrm{n}\rangle\right)^2 F_\mathrm{SD}^2(E_\mathrm{R}). \tag{12}$$

As before, $\sigma_\mathrm{p}^\mathrm{SD}$ denotes the WIMP-proton SD cross section and we have assumed that the coupling to protons and neutrons is equal ($a_n = a_p$). The total nuclear spin of the target is denoted J, while the expectation values of the proton and neutron spin operators are given by $\langle S_\mathrm{p}\rangle$ and $\langle S_\mathrm{n}\rangle$, respectively. The SD form factor can be written as

$$F_\mathrm{SD}^2(E_\mathrm{R}) = \frac{S(E_\mathrm{R})}{S(0)}, \tag{13}$$

where $S(E_\mathrm{R})$ describes the energy dependence of the recoil rate due to the fact that the nucleus is not composed of a single spin but rather a collection of spin-1/2 nucleons. This response function $S(E_\mathrm{R})$ is usually decomposed in terms of spin structure functions [51],

$$S(E_\mathrm{R}) = a_0^2 S_{00}(E_\mathrm{R}) + a_0 a_1 S_{01}(E_\mathrm{R}) + a_1^2 S_{11}(E_\mathrm{R}), \tag{14}$$

where $a_0 = a_\mathrm{p} + a_\mathrm{n}$ is the isoscalar coupling and $a_1 = a_\mathrm{p} - a_\mathrm{n}$ is the isovector coupling. Under the assumption $a_\mathrm{n} = a_\mathrm{p}$, then $a_0 = 2a_\mathrm{p}$ and $a_1 = 0$, and only the isoscalar structure function $S_{00}(E_\mathrm{R})$ will be relevant for our analysis.

The functional form for S_{ij} can be calculated from shell models for the nucleus [52]. However, competing models (such as the odd group model [53], interacting boson fermion model [54] and independent single particle shell model [55], among others) may lead to different spin structure functions, generating a significant uncertainty in the value of the SD cross section. This issue was explored by Ref. [56], who developed a parametrization for the spin structure functions in terms of the parameter $u = (qb)^2/2$, where

$$b = \sqrt{\frac{41.467}{(45.0A^{-1/3} - 25.0A^{-2/3})}}\ \mathrm{fm}, \tag{15}$$

is the oscillator size parameter [52,57]. Their parametrization takes the form

$$S_{ij} = N((1-\beta)\mathrm{e}^{-\alpha u} + \beta). \tag{16}$$

The values we use for the parameters (N, α, β) are (0.0595,3.75,0.0096) for ^{129}Xe, (0.035,3.925,0.12) for ^{131}Xe and (0.195,4.25,0.07) for ^{73}Ge. These values were chosen to approximately reproduce the median values obtained from a range of spin structure function calculations [52,58–60]. We keep the values of these parameters fixed in our analysis in order to focus on the impact of astrophysical uncertainties. We note that argon has zero spin and, therefore, has no SD interaction with WIMPs.

The proton and neutron spins $\langle S_\mathrm{p,n}\rangle$ can be rewritten in terms of the total nuclear spin and the spin structure functions (as in Ref. [61]). Using this to rewrite Eq. (12), gives the following expression (in the case $a_p = a_n$):

$$\frac{\mathrm{d}\sigma_\mathrm{SD}}{\mathrm{d}E_R} = \frac{8\pi m_N \sigma_\mathrm{p}^\mathrm{SD}}{3\mu_{\chi p}^2 v^2}\frac{S_{00}(E_R)}{(2J+1)}. \tag{17}$$

Both the SI and SD differential cross sections are inversely proportional to the WIMP velocity squared. Factoring out all the terms that do not depend on v in Eq. (2), the integral over the WIMP speed is normally written as $\eta(v_\mathrm{min})$:

$$\eta(v_\mathrm{min}) = \int_{v_\mathrm{min}}^{\infty} \frac{f_1(v)}{v}\mathrm{d}v, \tag{18}$$

and we will subsequently refer to this quantity as the velocity integral.

B. Neutrino telescopes

The WIMP capture rate per unit shell volume for a shell at distance r from the center of the Sun, due to species i is given by [62,63]

$$\frac{\mathrm{d}C_i}{\mathrm{d}V} = \int_0^{v_\mathrm{max}} \mathrm{d}v \frac{f_1(v)}{v} w\Omega^-_{w_\mathrm{esc},i}(w), \tag{19}$$

where v is the asymptotic WIMP speed,[1] $w(r) = \sqrt{v^2 + w_\mathrm{esc}(r)^2}$ and $w_\mathrm{esc}(r)$ is the local escape speed at radius r inside the Sun.[2] The rate per unit time at which a single WIMP traveling at speed w is scattered down to a speed less than w_esc, due to the interaction with species i, is $\Omega^-_{w_\mathrm{esc},i}(w)$. Finally, the upper limit of integration is given by

$$v_\mathrm{max} = \frac{\sqrt{4m_\chi m_{\mathrm{N}_i}}}{m_\chi - m_{\mathrm{N}_i}} w_\mathrm{esc}, \tag{20}$$

where m_{N_i} is the mass of the nucleus of species i. Above v_max, WIMPs cannot lose enough energy in a recoil to drop below the local escape speed and, therefore, they are not captured by the Sun.

The scatter rate $\Omega^-_{w_\mathrm{esc},i}$ from a species with number density n_{N_i} can be written as

$$\Omega^-_{w_\mathrm{esc},i}(w) = w n_{\mathrm{N}_i} \int_{E_v}^{E_\mathrm{max}} \frac{\mathrm{d}\sigma}{\mathrm{d}E_\mathrm{R}} \mathrm{d}E_\mathrm{R}, \tag{21}$$

where E_R is the energy lost by the scattering WIMP. The limits of integration run from the minimum energy loss required to reduce the WIMP speed below w_esc,

$$E_v = \frac{m_\chi}{2}(w^2 - w_\mathrm{esc}^2) = \frac{m_\chi}{2}v^2, \tag{22}$$

to the maximum possible energy loss in the collision,

$$E_\mathrm{max} = \frac{2\mu^2_{\chi \mathrm{N}_i}}{m_{\mathrm{N}_i}} w^2. \tag{23}$$

As in the direct detection case, we can decompose the differential cross section into SI and SD components. While all of the constituent elements of the Sun are sensitive to SI interactions, only spin-1/2 hydrogen is sensitive to SD scattering. The differential cross section is, therefore, given by

---

[1] In the literature, the asymptotic WIMP speed is typically written as u. Here, we denote it as v for consistency with the notation of the direct detection formalism.

[2] For compactness, we subsequently suppress the radial dependence when denoting $w(r)$ and $w_\mathrm{esc}(r)$.

$$\frac{\mathrm{d}\sigma}{\mathrm{d}E_\mathrm{R}} = \frac{m_{\mathrm{N}_i}}{2\mu_{\chi\mathrm{p}}^2 v^2} \times \begin{cases} \sigma_\mathrm{p}^\mathrm{SI} + \sigma_\mathrm{p}^\mathrm{SD} & \text{for } A = 1, \\ \sigma_\mathrm{p}^\mathrm{SI} A_i^2 F_i^2(E_\mathrm{R}) & \text{for } A > 1. \end{cases} \tag{24}$$

No form factor is needed for hydrogen, which consists of only a single nucleon. For the remaining nuclei, we approximate the form factor as [62]

$$F_i^2(E_\mathrm{R}) = \exp\left(-\frac{E_\mathrm{R}}{E_i}\right), \tag{25}$$

$$E_i = \frac{3}{2m_{\mathrm{N}_i} R_i^2}. \tag{26}$$

This allows Eq. (21) to be calculated analytically and introduces an error in the total capture rate of only a few percent.

Figure 1 shows the maximum solar capture speed v_max given by Eq. (20) (averaged over the solar radius). We consider separately the SD contribution (dashed red line) from hydrogen and the SI contribution (solid red line) averaged over all elements in the Sun. The former goes from a value slightly larger than 1000 $\mathrm{km\,s^{-1}}$ for a 10 GeV WIMP down to ~100 $\mathrm{km\,s^{-1}}$ for a mass of 1 TeV, while the latter is larger by a factor of approximately two. The sharp peaks in the SI curve for v_max are resonances due to mass matching between the WIMP and one of the nuclei in the Sun. In these cases, energy transfer during recoils can be very efficient and WIMPs with high speeds can be captured.

The two red lines should be compared with the blue (green hatched) band, which shows the velocity window to which a xenon-based (argon-based) experiment is sensitive (assuming the energy thresholds described in Sec. III and Table I). We note that, over the whole range of masses considered, the maximum solar capture speed is always larger (both for SI and SD interactions) than the lower edge of the blue band. This means that, as anticipated in the introduction, neutrino telescopes are sensitive to all of the low-speed tail of the velocity distribution that is inaccessible to direct detection experiments.

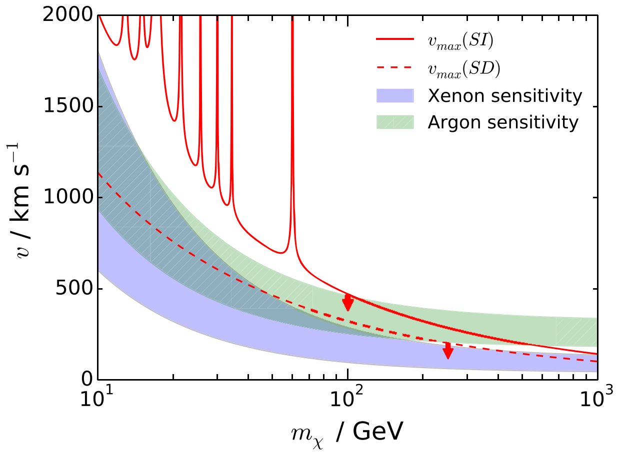

FIG. 1 (color online). The ranges of WIMP velocity that solar capture and direct detection experiments are sensitive to, as a function of the WIMP mass. The blue band shows the range of speeds to which a xenon-based detector with an energy window of [5,45] keV is sensitive. The green hatched band shows the corresponding range of speeds for an argon-based detector with an energy window of [30,100] keV. The solid (dashed) red lines shows the maximum speed to which solar WIMP capture is sensitive for SI (SD) interactions. See the text for further details.

TABLE I. Summary of the parameters describing the mock direct detection experiments. All experiments have a constant energy resolution of $\sigma_E = 1$ keV and a flat background rate of 10^{-7} events/kg/day/keV. The energy windows are chosen to be similar to those proposed in Refs. [64,65] and [66] for xenon, germanium and argon, respectively. We assume natural isotopic abundances of the target materials.

Experiment	Energy Range (keV)	Exposure (ton-yr)	Energy bin width (keV)
Xenon	5–45	1.0	2.0
Argon	30–100	1.0	2.0
Germanium	10–100	0.3	2.0

WIMPs which are captured can annihilate in the Sun to Standard Model particles. Over long timescales, equilibrium is reached between the capture and annihilation rates. In such a regime, the annihilation rate Γ_A is equal to half the capture rate, independent of the unknown annihilation cross section [39]. For large enough scattering cross sections ($\sigma_\mathrm{p}^\mathrm{SD} \gtrsim 10^{-43}$ cm^2), capture is expected to be efficient enough for equilibrium to be reached [67]. The assumption of equilibrium is, therefore, reasonable for the benchmarks considered in this work.

The majority of Standard Model particles produced by WIMP annihilations cannot escape the Sun. However, some of these particles may decay to neutrinos or neutrinos may be produced directly in the annihilation. Neutrinos can reach the Earth and be detected by neutrino telescope experiments. In this work, we focus on the IceCube experiment [68], which measures the Čerenkov radiation produced by high energy particles traveling through ice. IceCube aims at isolating the contribution of muons produced by muon neutrinos interacting in the Earth or its atmosphere. The amount of Čerenkov light detected, combined with the shape of the Čereknow cascade, allows the energy and direction of the initial neutrino to be reconstructed.

The spectrum of neutrinos arriving at IceCube is given by

$$\frac{\mathrm{d}N_\nu}{\mathrm{d}E_\nu} = \frac{\Gamma_A}{4\pi D^2} \sum_f B_f \frac{\mathrm{d}N_\nu^f}{\mathrm{d}E_\nu}, \tag{27}$$

where D is the distance from the Sun to the detector and the sum is over all annihilation final states f, weighted by the branching ratios B_f. The factor $\mathrm{d}N_\nu^f/\mathrm{d}E_\nu$ is the neutrino spectrum produced by final state f, taking into account the propagation of neutrinos as they travel from the Sun to the detector [69,70]. The branching ratios depend on the specific WIMP under consideration. For simplicity, it is typically assumed (as we do here) that the WIMPs annihilate into a single channel. For the computation of Eq. (27) we use a modified version of the publicly available DarkSUSY code [71,72], that also accounts for the telescope efficiency (see also Sec. III).

III. BENCHMARKS AND PARAMETER RECONSTRUCTION

In order to determine how well the WIMP parameters can be recovered, we generate mock data sets for IceCube and three hypothetical direct detection experiments.

Table I displays the parameters we use for the three direct detection experiments. They are chosen to broadly mimic next-generation detectors that are currently in development. Each experiment is described by the energy window it is sensitive to and the total exposure, which is the product of the fiducial detector mass, the exposure time and the experimental and operating efficiencies (which we implicitly assume to be constant). We also include a gaussian energy resolution of $\sigma_E = 1$ keV[3] and a flat background rate of 10^{-7} events/kg/day/keV.

We choose three experiments using different target nuclei as it has been shown that the employment of multiple targets significantly enhances the accuracy of the reconstruction of the WIMP mass and cross sections [74–76]. Furthermore, if the WIMP velocity distribution is not known, multiple targets are a necessity [31]. For more details on the reconstruction performance of different ensembles of target materials, we refer to reader the Ref. [30]. We note that our modeling of the detectors is rather unsophisticated. More realistic modeling would include, for instance, energy-dependent efficiency. However, the detector modeling we employ here is sufficient to estimate the precision with which the WIMP parameters can be recovered.

We divide the energy range of each experiment into bins and generate Asimov data [77] by setting the observed number of events in each bin equal to the expected number of events. While this cannot correspond to a physical realization of data as the observed number of events will be noninteger, it allows us to disentangle the effects of Poissonian fluctuations from the properties of the parametrizations under study. Including the effect of Poissonian fluctuations would require the generation of a large number of realizations for each benchmark. The precision in the reconstruction of the WIMP parameters will, in general, be different for each realization. This leads to the concept of *coverage*, i.e. how many times the benchmark value is contained in the credible interval estimating the uncertainty in the reconstruction (c.f. Ref. [78]). We leave this for future work, noting here that Ref. [33] showed that the polynomial parametrization we use (Sec. III B) provides almost exact coverage for the reconstruction of the WIMP mass (at least in the case of $m_\chi = 50$ GeV).

For the mock neutrino telescope data, we consider the IceCube 86-string configuration. We follow Ref. [41] and use an exposure time of 900 days (corresponding to five 180-days austral Winter observing seasons) and an angular cut around the solar position of $\phi_{\mathrm{cut}} = 3°$. This value is chosen to reflect the typical angular resolution of the IceCube detector [79] and has previously been shown to be the optimal angular cut over a range of DM masses [80]. This results in approximately 217 background events over the full exposure. As with the direct detection experiments, we set the observed number of events equal to the expected number of signal plus background events. We use only the observed number of events as data and not their individual energies. While event-level likelihood methods have previously been developed [81] for the use of IceCube 22-string data [82], a similar analysis has not yet been performed for IceCube-86. In particular, the probability distributions for the number of lit digital optical modules as a function of neutrino energy are not yet available for IceCube-86. Nonetheless, using only the number of observed events is a first step towards the characterization of the WIMP speed distribution with neutrino telescopes.

A. Benchmarks

The four benchmark models we use to generate mock data sets are summarized in Table II, along with the number of events produced in each experiment. In all cases, we use a SI WIMP-proton cross section of $\sigma_{\mathrm{p}}^{\mathrm{SI}} = 10^{-45}$ cm^2 and a SD cross section of $\sigma_{\mathrm{p}}^{\mathrm{SD}} = 2\times 10^{-40}$ cm^2, both of which are close to the current best exclusion limits [83,84].

The WIMPs in benchmarks A and B have an intermediate mass of 100 GeV and the production of neutrinos originates from annihilations into W^+W^-. This is a similar configuration to benchmark B used by Ref. [41]. For benchmarks C and D we decrease the mass to 30 GeV, which allows a more accurate reconstruction of the WIMP mass (see Secs. IV and V). The IceCube detector (with DeepCore) is sensitive to WIMPs with masses down to about 20 GeV [85]. For benchmarks C and D we assume that annihilations take place directly into $\nu_\mu\bar{\nu}_\mu$.

Other annihilation channels may produce fewer neutrinos and, thus, reduce the impact of IceCube in the reconstruction of the particle physics nature of DM and its $f(v)$. However, note that, according to Ref. [86],

---

[3] The precise value of σ_E is not expected to strongly affect parameter reconstruction, unless $\sigma_E > E_{\mathrm{th}}$ [73].

TABLE II. Summary of the WIMP benchmarks. The first section shows the WIMP mass, speed distribution and annihilation channel. SHM refers to the Standard Halo Model, with a speed distribution described by Eq. (1) with $v_{\mathrm{lag}} = 230\ \mathrm{km\,s^{-1}}$ and $\sigma_v = 163\ \mathrm{km\,s^{-1}}$. In the case of SHM + DD, we also include the contribution of a dark disk, described by an additional term as in Eq. (1), but with $v_{\mathrm{lag}} = 50\ \mathrm{km\,s^{-1}}$ and $\sigma_v = 50\ \mathrm{km\,s^{-1}}$. For all benchmarks, we consider only isospin-conserving interactions (i.e. $f_{\mathrm{p}} = f_{\mathrm{n}}$ and $a_{\mathrm{p}} = a_{\mathrm{n}}$) and assume $\sigma_{\mathrm{p}}^{\mathrm{SI}} = 10^{-45}\ \mathrm{cm}^2$ and $\sigma_{\mathrm{p}}^{\mathrm{SD}} = 2\times10^{-40}\ \mathrm{cm}^2$. The second section gives the number of events produced in the xenon-, argon- and germanium-based direct detection experiments (with the number of recoils induced by SI and SD interactions listed separately) and IceCube.

Benchmark	m_χ(GeV)	Speed dist.	Annihilation channel	N_{Xe}(SI)	N_{Xe}(SD)	N_{Ar}(SI)	N_{Ar}(SD)	N_{Ge}(SI)	N_{Ge}(SD)	N_{IC}
A	100	SHM	W^+W^-	154.9	262.7	16.1	0	25.4	18.7	43.3
B	100	SHM + DD	W^+W^-	167.1	283.9	16.2	0	25.7	18.9	242.9
C	30	SHM	$\nu_\mu\bar{\nu}_\mu$	175.1	301.1	6.2	0	20.5	16.1	13.2
D	30	SHM + DD	$\nu_\mu\bar{\nu}_\mu$	175.0	300.9	5.8	0	20.4	16.0	40.2

the only annihilation channels not decaying with a significant probability into neutrinos are electrons, gluons and gamma rays. The scan of nonminimal supersymmetry performed in Ref. [87] showed that these are subdominant channels.

Benchmarks A and C assume a SHM speed distribution as described in Sec. II, with $v_{\mathrm{lag}} = 230\ \mathrm{km\,s^{-1}}$ [6,88] and $\sigma_v = 163\ \mathrm{km\,s^{-1}}$. Benchmarks B and D also include a moderate dark disk with a population of low-speed WIMPs which contribute an additional 30% to the local DM density. We assume that the dark disk velocity distribution is also given by Eq. (1), with $v_{\mathrm{lag}} = 50\ \mathrm{km\,s^{-1}}$ and $\sigma_v = 50\ \mathrm{km\,s^{-1}}$ [89]. As shown in Ref. [90], the capture rate in the Sun is not affected by variations in the shape of $f(v)$ (such as the differences between distribution functions extracted from different N-body simulations). However, significant enhancement of the capture rate can occur if there is a dark disk [89], and our benchmarks have been chosen in order to investigate this scenario. Finally, we assume a fixed value for the SHM local DM density of $\rho_0 = 0.3\ \mathrm{GeV\,cm^{-3}}$. There is an uncertainty in this value of around a factor of 2 (see e.g. Refs. [91–95]). However, this is degenerate with the cross sections.

In this work, we assume a common speed distribution $f(v)$ experienced by both Earth-based experiments and by the Sun. In principle, gravitational focussing and diffusion could lead to differences between the forms of $f(v)$ at the Earth and Sun [67,96]. However, a recent study using Liouville's theorem showed that such effects must be balanced by inverse processes [97]. We can, therefore, treat the WIMP population as being effectively free and consider only a single common form for $f(v)$.

B. Parametrizations of the speed distribution

We use the mock data generated for the benchmarks in Table II to evaluate the likelihood employed in the Bayesian scans over m_χ, $\sigma_{\mathrm{p}}^{\mathrm{SI}}$ and $\sigma_{\mathrm{p}}^{\mathrm{SD}}$. In order to study the synergy between direct detection experiments and neutrino telescopes in the reconstruction of the speed distribution, some of these scans will also include parameters which describe the form of $f(v)$. We consider two possible parametrizations:

(i) **Binned parametrization:** This parametrization was introduced in Ref. [4] and it involves dividing $f(v)$ into N bins of width Δv with bin edges $\tilde{v}_i$ and parametrizing the bin heights by g_i,

$$f(v) = \sum_{i=1}^{N} \frac{3 g_i W(v; \tilde{v}_i, \Delta v)}{(\tilde{v}_i + \Delta v)^3 - \tilde{v}_i^3}, \tag{28}$$

where the top-hat function, W, is defined as

$$W(v; \tilde{v}_i, \Delta v) = \begin{cases} 1 & v \in [\tilde{v}_i, \tilde{v}_i + \Delta v], \\ 0 & \text{otherwise.} \end{cases} \tag{29}$$

The bin heights then satisfy the normalization condition

$$\sum_{i=1}^{N} g_i = 1. \tag{30}$$

We parametrize $f(v)$ up to some maximum speed $v_{\max} = N\Delta v$, above which we set $f(v) = 0$. We choose $v_{\max} = 1000\ \mathrm{km\,s^{-1}}$, conservatively larger than the escape velocity in the Earth frame, which is around $800\ \mathrm{km\,s^{-1}}$ [7,8]. The binned parametrization was studied in detail in Ref. [31], where it was demonstrated that, when only direct detection data are used, this method results in a bias towards smaller WIMP masses.

(ii) **Polynomial parametrization:** In Ref. [32] we proposed that the natural logarithm of $f(v)$ be expanded in a series of polynomials in v, i.e.

$$f(v) = \exp\left[\sum_{k=0}^{N-1} a_k P_k(2v/v_{\max} - 1)\right]. \tag{31}$$

The first coefficent a_0 is fixed by requiring the speed distribution to be normalized to 1. As detailed in Ref. [33], various polynomial bases can be used. Chebyshev and Legendre polynomials allow an unbiased reconstruction of the WIMP mass across a wide range of astrophysical and particle physics benchmarks [32,33], and the scans are normally faster if Chebyshev polynomials are used. We, therefore, use a basis of N Chebyshev polynomials P_k weighted by the parameters a_k.

By studying two different speed parametrizations, we can examine how particle physics parameter reconstruction is affected by the choice of speed parametrization. While the binned parametrization may lead to a bias in the WIMP mass, it is straightforward and provides a good approximation to smoothly varying speed distributions. As discussed in Ref. [31], this bias is due in part to a lack of information about $f(v)$ at low speeds. We, therefore, expect that the addition of IceCube data will reduce this bias. By comparison, the polynomial distribution is unbiased and allows for a wider range of shapes for $f(v)$, although some of these are rapidly varying and may not be physically well motivated. For a large number of parameters, these two methods should converge and both could be used as a consistency check.

C. Parameter sampling

We perform parameter scans using a modified version of the publicly available MultiNest 3.6 package [98–100]. This allows us to map out the likelihood $\mathcal{L}(\mathbf{\Theta})$ for the model parameters $\mathbf{\Theta}$. We use $N_{\mathrm{live}} = 20,000$ live points and a tolerance of 10^{-4}. The priors we use for the various parameters are displayed in Table III.

Due to the normalization condition on the bin heights [given in Eq. (30)] for the case of the binned parametrization of $f(v)$, we must sample these parameters from the so-called "simplex" priors; i.e., we uniformly sample $\{g_2, \ldots, g_N\}$ such that they sum to less than one and then fix g_1 as

$$g_1 = 1 - \sum_{i=2}^{N} g_i. \tag{32}$$

TABLE III. Summary of prior types and ranges. The "simplex" prior is described in Sec. III C.

Parameter	Prior range	Prior type
m_χ (GeV)	10–1000	log-flat
$\sigma_{\mathrm{p}}^{\mathrm{SI}}$ (cm^2)	10^{-48}–10^{-42}	log-flat
$\sigma_{\mathrm{p}}^{\mathrm{SD}}$ (cm^2)	10^{-43}–10^{-37}	log-flat
Polynomial coefficients $\{a_k\}$	−20–20	linear-flat
Bin heights $\{g_i\}$	0–1	simplex

The ellipsoidal sampling performed by MultiNest becomes increasingly inefficient as the number of bins N increases, since the volume of the parameter space for which Eq. (30) is satisfied becomes very small. We, therefore, use MultiNest in constant efficiency mode when using the binned parametrization, with a target efficiency of 0.3. We use a total of ten bins in this parametrization (nine free parameters, with one fixed by normalization), which should allow us to obtain a close approximation to the rapidly varying SHM + DD distribution.

For the polynomial $\ln f(v)$ parametrization, we use six basis polynomials (five free coefficients, with one fixed by normalization). This is a smaller number of parameters than for the binned parametrization because the polynomial coefficients are allowed to vary over a much wider range. The volume of the polynomial parameter space is, therefore, significantly larger than for the binned parametrization and a much larger number of live points would be required to accurately map the likelihood using ten parameters. As we will see, using six basis functions still allows a wide range of speed distributions to be explored and provides a good fit to the data (see also the discussion in Ref. [33]). With a larger numbers of events, it would be feasible to increase the number of basis functions and more precisely parametrize the form of the speed distribution.

The likelihood function we use for each experiment is

$$\mathcal{L}(\mathbf{\Theta}) = \prod_{i=1,N_{\mathrm{bins}}} \frac{(N_{\mathrm{e}}^i)^{N_{\mathrm{o}}^i}}{N_{\mathrm{o}}^i!} e^{-N_{\mathrm{e}}^i}, \tag{33}$$

where the energy window is divided into N_{bins} bins. For each bin, N_{e}^i is the expected number events, for a given set of parameters $\mathbf{\Theta}$, and N_{o}^i is the observed number of events (i.e. the mock data). The total likelihood is the product over the likelihoods for each experiment considered.

Finally, it is often interesting to consider the probability distribution of a subset of parameters from the full parameter space. We do this by *profiling*, so that the profile likelihood $\mathcal{L}_p(\theta_i)$ of the ith parameter is obtained by maximizing $\mathcal{L}$ over the other parameters:

$$\mathcal{L}_p(\theta_i) = \max_{0,\ldots,i-1,i+1,\ldots,N} \mathcal{L}(\mathbf{\Theta}). \tag{34}$$

We have checked that, for the data sets and likelihoods used here, the marginalized posterior distributions of the parameters of interest do not differ qualitatively from the profile likelihood. We, therefore, do not display the marginalized posterior distributions. Because we only make use of the likelihood (and not the posterior distribution) in parameter inference, we expect that the priors will not strongly impact the results. In addition, the use of Asimov data with a large number of energy bins means that we expect the confidence intervals obtained from the asymptotic properties of the profile likelihood to be valid.

IV. DIRECT DETECTION DATA ONLY

In this section we present the results of the scans performed with only direct detection data, leaving the discussion of the impact of IceCube data for the following section.

A. Benchmark A

Figure 2 shows the two-dimensional profile likelihood distributions for benchmark A, i.e. $m_\chi = 100$ GeV, $\sigma_\mathrm{p}^\mathrm{SI} = 10^{-45}$ cm^2, $\sigma_\mathrm{p}^\mathrm{SD} = 2 \times 10^{-40}$ cm^2 and a SHM $f(v)$. Left panels are for $(m_\chi, \sigma_\mathrm{p}^\mathrm{SI})$, central ones for $(m_\chi, \sigma_\mathrm{p}^\mathrm{SD})$, while the ones on the right are for $(\sigma_\mathrm{p}^\mathrm{SI}, \sigma_\mathrm{p}^\mathrm{SD})$. Shaded regions and solid blue contours are for scans carried out over particle physics quantities (i.e. m_χ, $\sigma_\mathrm{p}^\mathrm{SI}$ and $\sigma_\mathrm{p}^\mathrm{SD}$) as well as the parameters entering in the parametrization of the speed distribution. The first row is for the binned $f(v)$ and the second row for the polynomial expansion (see Sec. III B). In addition, the dashed black contours are from a scan performed keeping the speed distribution fixed, i.e. assuming that the correct $f(v)$ is known and there are no astrophysical uncertainties.

In the case of a fixed speed distribution (dashed black lines), the reconstruction is very good: the mass is well constrained and closed contours are obtained for both the SI and SD cross section (right column). These constraints on the WIMP mass are similar to those obtained in Ref. [41] whose Benchmark B is the same as our Benchmark A (see the middle row of Fig. 1 of Ref. [41]). However, the possible degeneracy between the two cross sections [75], which is observed in Ref. [41], is broken by the fact that we use three different target experiments, one of which (argon) is only sensitive to SI interactions.

When we allow for the realistic possibility of a variable speed distribution, the contours unsurprisingly increase in size. For both the binned and polynomial parametrization, the contours have a similar shape, extending down to 20–30 GeV in m_χ. This is because both parametrizations

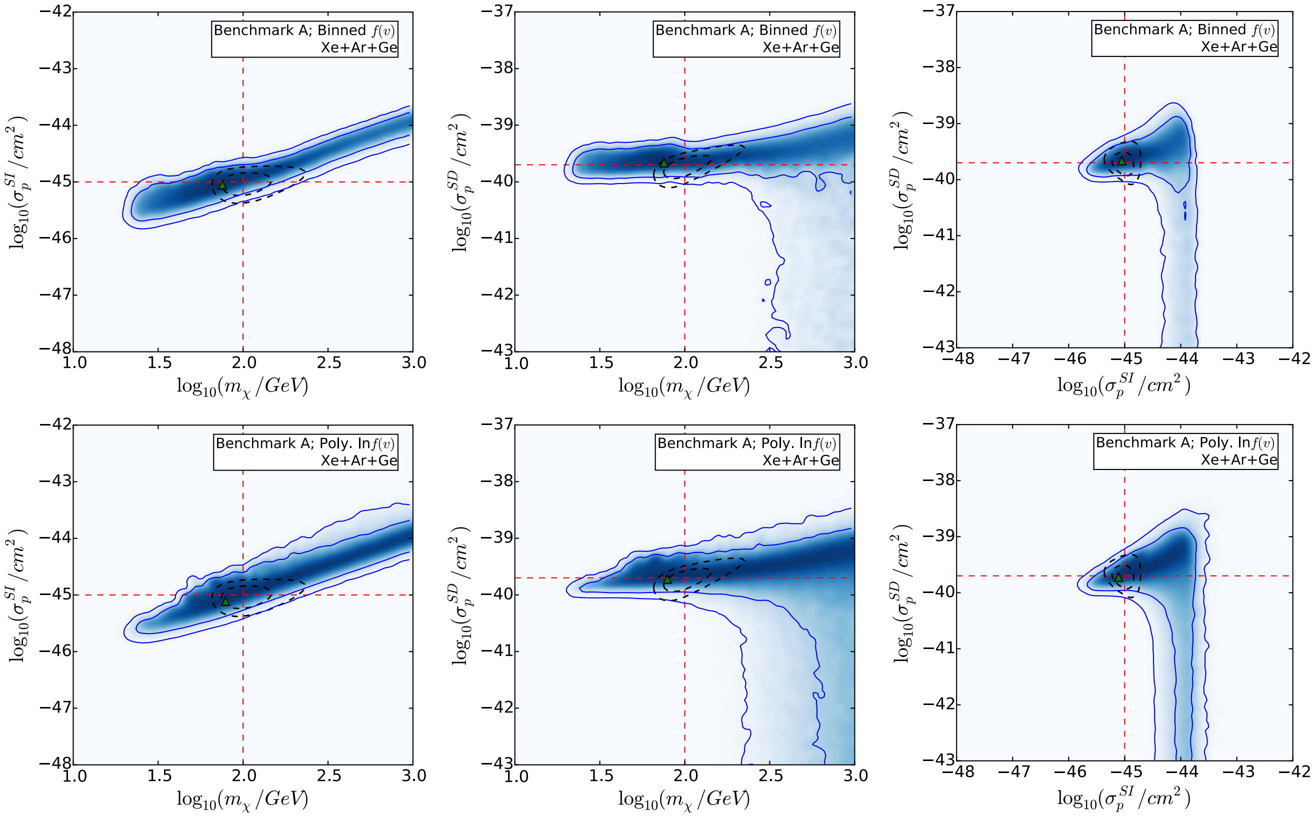

FIG. 2 (color online). Two-dimensional profile likelihood for $(m_\chi, \sigma_\mathrm{p}^\mathrm{SI})$ (left column), $(m_\chi, \sigma_\mathrm{p}^\mathrm{SD})$ (central column) and $(\sigma_\mathrm{p}^\mathrm{SI}, \sigma_\mathrm{p}^\mathrm{SD})$ (right column), using only information from three direct detection experiments with xenon, germanium and argon targets (see Table I) for benchmark A. The shaded areas and solid blue contours are obtained from a scan of a parameter space that includes both the particle physics quantities (m_χ, $\sigma_\mathrm{p}^\mathrm{SI}$ and $\sigma_\mathrm{p}^\mathrm{SD}$) and the parameters defining the speed distribution. The panels in the top row are for a binned parametrization, while those in the second row are for a polynomial parametrization (see Sec. III). The dashed black contours are from a separate scan, performed with the speed distribution fixed to its input form (see Table II). In all cases, the inner (outer) contours enclose the 68% (95%) confidence level region. The green triangle marks the position of the best-fit point for the scan including the parameters of the speed distributions. The red dashed lines show the nominal values for m_χ, $\sigma_\mathrm{p}^\mathrm{SI}$ and $\sigma_\mathrm{p}^\mathrm{SD}$ assumed for this benchmark.

can encompass distributions that are flatter than the SHM. Decreasing the WIMP mass steepens the recoil spectrum, allowing these flatter distributions to be compatible with the mock data. An example of such a speed distribution is the one labeled "i" in Fig. 3. In order to remain normalized, such distributions must be depleted at low speeds (i.e. below 200 $\mathrm{km\,s^{-1}}$), where the experiments are no longer sensitive (see Fig. 1).

Similarly, the data can also be well fit by higher WIMP masses. Increasing the WIMP mass moves the v_{min} intervals probed by the three direct detection experiments to lower values (see Fig. 1). However, in order to provide a good fit to the data, the relative number of recoil events in each experiment must remain roughly the same. With the SHM, this is not possible, since too few events would be produced in the xenon experiment. A velocity integral which is similar to the SHM in the region probed by germanium and argon, but steeper in the region probed by xenon can be used to compensate for this by increasing the number of xenon events. An example of a speed distribution which produces this effect is shown in Fig. 3, labeled "ii." Such an $f(v)$ is possible with both the polynomial and binned parametrization and, therefore, larger WIMP masses are allowed. Furthermore as m_χ is increased above the masses of the target nuclei, the shape of the recoil spectrum becomes almost independent of m_χ. This effect is well understood [73,101] and it contributes to the degeneracy between the mass and the cross section for large m_χ. As a consequence of this effect, we also do not expect the results obtained here to change qualitatively if the upper limit of the prior were increased beyond 1000 GeV.

For large values of m_χ the contours also extend down to small values of $\sigma_{\mathrm{p}}^{\mathrm{SD}}$. This means that in the ($\sigma_{\mathrm{p}}^{\mathrm{SI}}$, $\sigma_{\mathrm{p}}^{\mathrm{SD}}$) plane the contours are now open (lower right panel), as opposed to the closed contours obtained with fixed astrophysics. As explained in the previous paragraphs, the region at large mass and large SI and SD cross sections provides a good fit to the data with a velocity integral that is slightly steeper than the SHM. Decreasing $\sigma_{\mathrm{p}}^{\mathrm{SD}}$ means that fewer events will be produced in the xenon and germanium experiments, with no effect on the argon detector. The same relative numbers of events for the three targets can be maintained with a velocity integral that is even steeper at low speeds (where xenon and germanium are sensitive), but unchanged in the region probed by argon, between 200 and 400 $\mathrm{km\,s^{-1}}$. This requires a shape for $f(v)$ which rises more rapidly at low speeds than example 'ii' in Fig. 3. With decreasing $\sigma_{\mathrm{p}}^{\mathrm{SD}}$, a point is reached where all the events are explained by SI interactions and lowering the SD cross section further has no effect. Conversely, it is not possible to explain the data in terms of only SD interactions, as $\sigma_{\mathrm{p}}^{\mathrm{SI}}$ is constrained by the (small) number of events in the argon experiment which couples only via SI interactions. Therefore, the contours do not extend to low values of $\sigma_{\mathrm{p}}^{\mathrm{SI}}$.

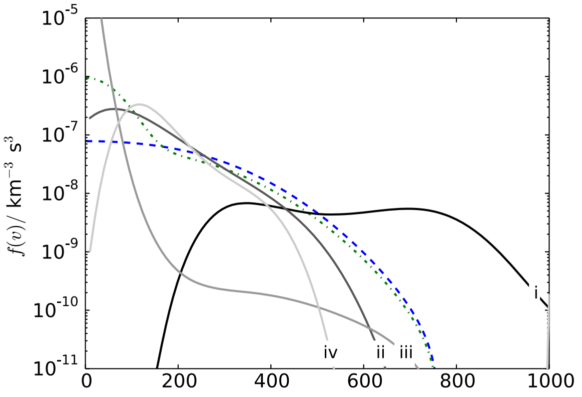

FIG. 3 (color online). Example shapes for the directionally-averaged velocity distribution $f(v)$. These are labeled i-iv and are referred to in the text of Sec. IV, V and VI to explain the different regions of parameter space which can be fit to the data. For comparison, the Standard Halo Model (SHM) and the SHM with a dark disk (SHM + DD) are shown as dashed blue and dot-dashed green lines, respectively.

B. Benchmark B

Figure 4 shows the two-dimensional profile likelihood distributions in the case of benchmark B, which has the same values of the particle physics parameters as benchmark A, but the input speed distribution includes a dark disk. The results for benchmark B with the speed distribution fixed to its input form (dashed black) are similar to those for benchmark A. However, the 95% confidence contours now extend up to large WIMP masses (left and central panels). When the WIMP mass is increased, the relative number of events in the xenon experiment can be too small. However, in benchmark B (unlike benchmark A) this is counteracted by the steep velocity integral at low speeds, due to the presence of the dark disk.

Again, when we allow the speed distribution to vary, the contours are significantly wider. In the case of the binned speed distribution, the likelihood peaks at around $m_\chi \approx 50$ GeV, compared to the input value of 100 GeV. A possible bias in the WIMP mass when using the binned distribution has been noted previously [4,31], although in this case the effect is relatively minor and the input value lies within the 68% contours. When the polynomial parametrization is used, the best-fit point is closer to the input parameter values. However, there is a strong degeneracy between the mass and the cross sections, and consequently for both parametrizations the displacement of the best-fit point away from the input parameter values is much smaller than the uncertainties on the parameters.

A significant difference between the two parametrizations is that the contours for the polynomial parametrization extend up to large values of $\sigma_{\mathrm{p}}^{\mathrm{SI}}$ and $\sigma_{\mathrm{p}}^{\mathrm{SD}}$ (this is most apparent in the lower-right panel of Fig. 4). This is a

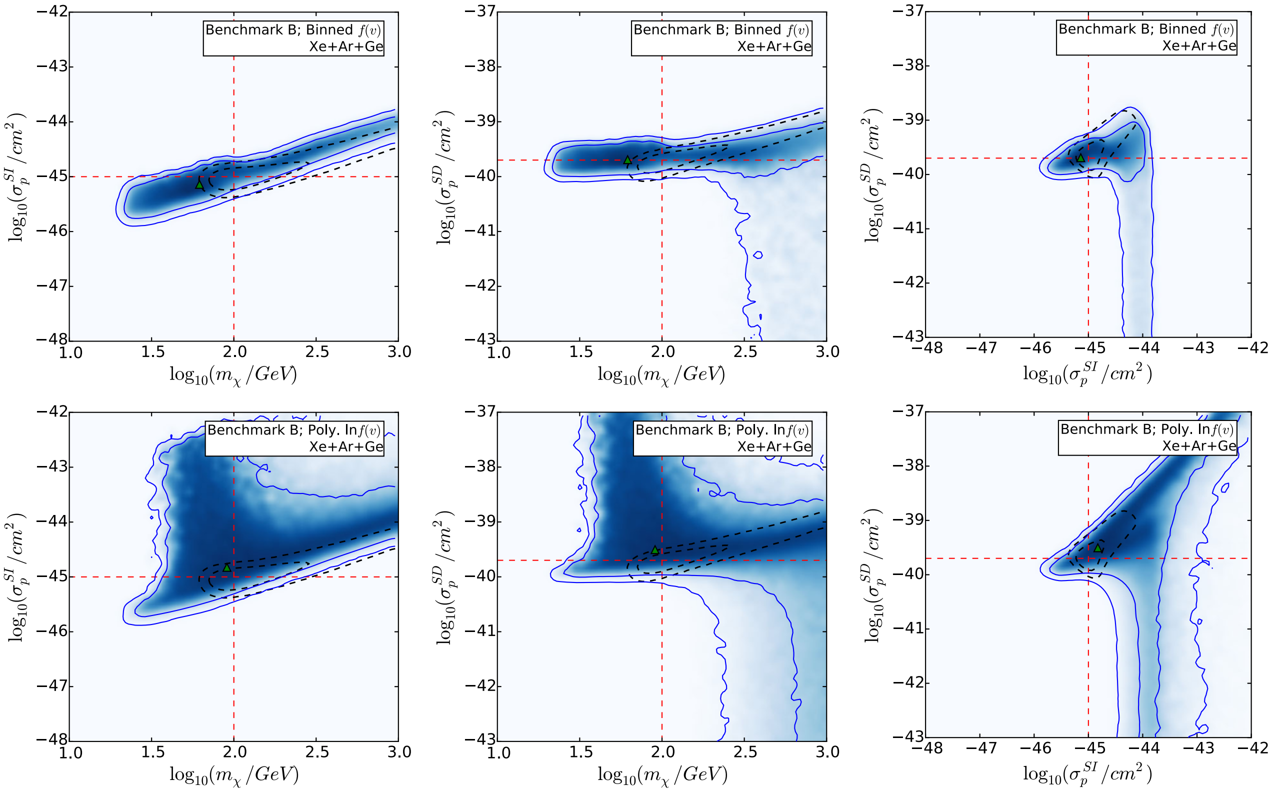

FIG. 4 (color online). Same as Fig. 2 but for benchmark B.

manifestation of the degeneracy described in Sec. I. Direct detection experiments do not probe the low-speed WIMP population. Thus, a velocity integral which is compatible with the input one in the region probed by the experiments but sharply increasing towards low speeds can still produce a good fit, provided that the cross section is also increased to give the correct total number of events. An example of such a distribution is shown in Fig. 3, labeled "iii." These rapidly varying distributions are more easily accommodated in the polynomial parametrization than in the binned one, which explains why the contours do not extend to large cross sections in that case (top row).

This region at large cross sections for the polynomial parametrization did not appear in the case of benchmark A. This is because the parameter space describing the shape of the speed distribution is very large and distribution functions which rise rapidly at low v do not make up a large fraction of the parameter space and, therefore, may not be well explored. In the case of benchmark B (which has a dark disk component), the input $f(v)$ is already increasing towards low speeds. This means that such rapidly rising distributions are better explored and this degeneracy becomes clear. The degeneracy up to high cross sections would become manifest for benchmark A if significantly more live points were used in the parameter scan. Therefore, the boundaries of the contours in Fig. 2 for benchmark A at large σ_p^{SI} and σ_p^{SD} should be considered as lower limits.

C. Benchmark C

Figure 5 shows the results for benchmark C, for which the mass is reduced to 30 GeV, with cross sections of $\sigma_p^{SI} = 10^{-45}$ cm^2 and $\sigma_p^{SD} = 2 \times 10^{-40}$ cm^2 and a SHM $f(v)$. As for benchmarks A and B, using a fixed speed distribution (black dashed) leads to closed contours and tight constraints on the WIMP parameters and, with the binned parametrization (top row), there again appears to be a slight bias towards lower WIMP masses, although the contours are not significantly widened. Indeed, for a binned $f(v)$, the reconstruction works quite well and all three quantities are determined with a good precision (approximately 1 order of magnitude for the cross sections and a factor of 2 for the WIMP mass). However, the results of the scan using the polynomial parametrization (bottom row) are dramatically different. The 95% confidence contours now extend up to $m_\chi \approx 100$ GeV, owing to the wide range of functional forms which can be explored by this parametrization. The degeneracy in the cross sections up to large values is even more pronounced than in the case of benchmark B. The lower input WIMP mass of benchmark C means that the region not covered by direct detection experiments extends up to $v \sim 200$ km s^{-1}, giving more freedom to the velocity integral to increase at low v.

For the polynomial parametrization, the contours extend down to arbitrarily small values of σ_p^{SD}. As in the case of the higher mass benchmarks, explaining the data with only SI interactions requires a steeper velocity integral. For the low

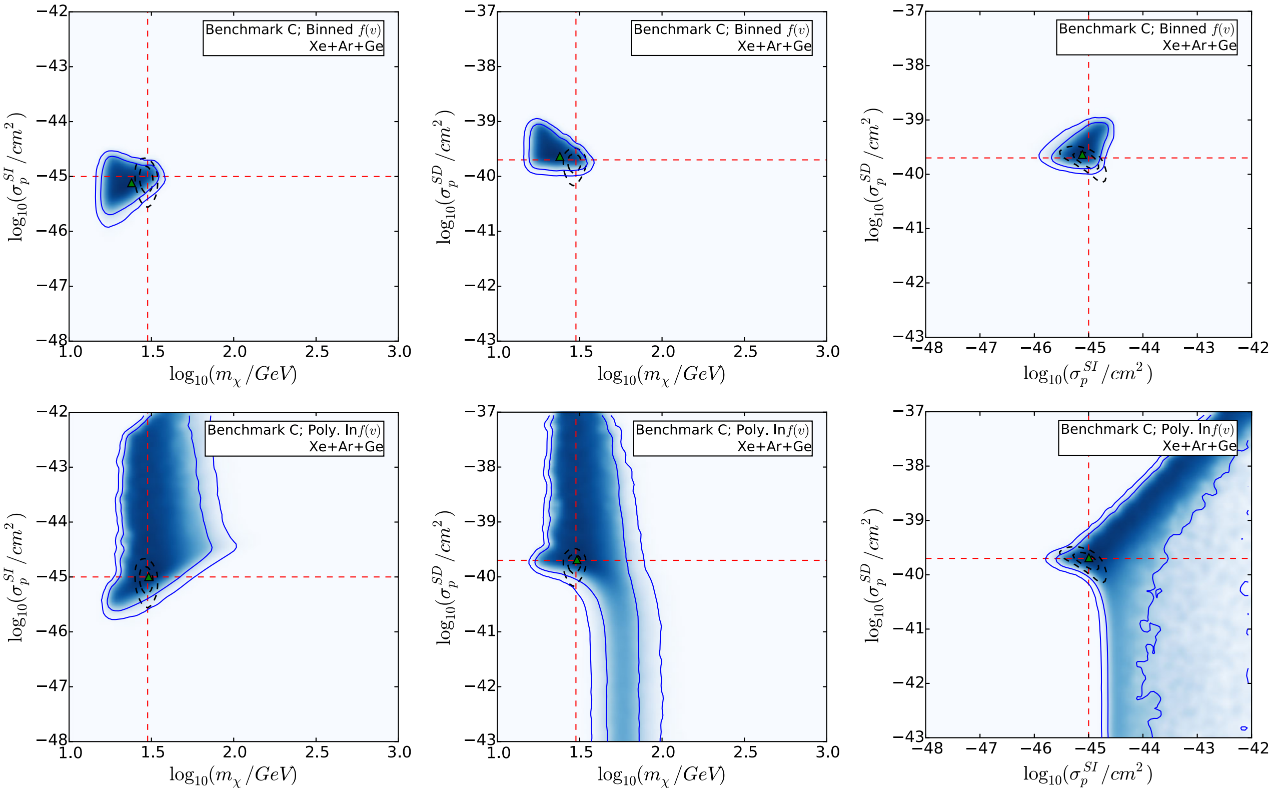

FIG. 5 (color online). Same as Fig. 2 but for benchmark C.

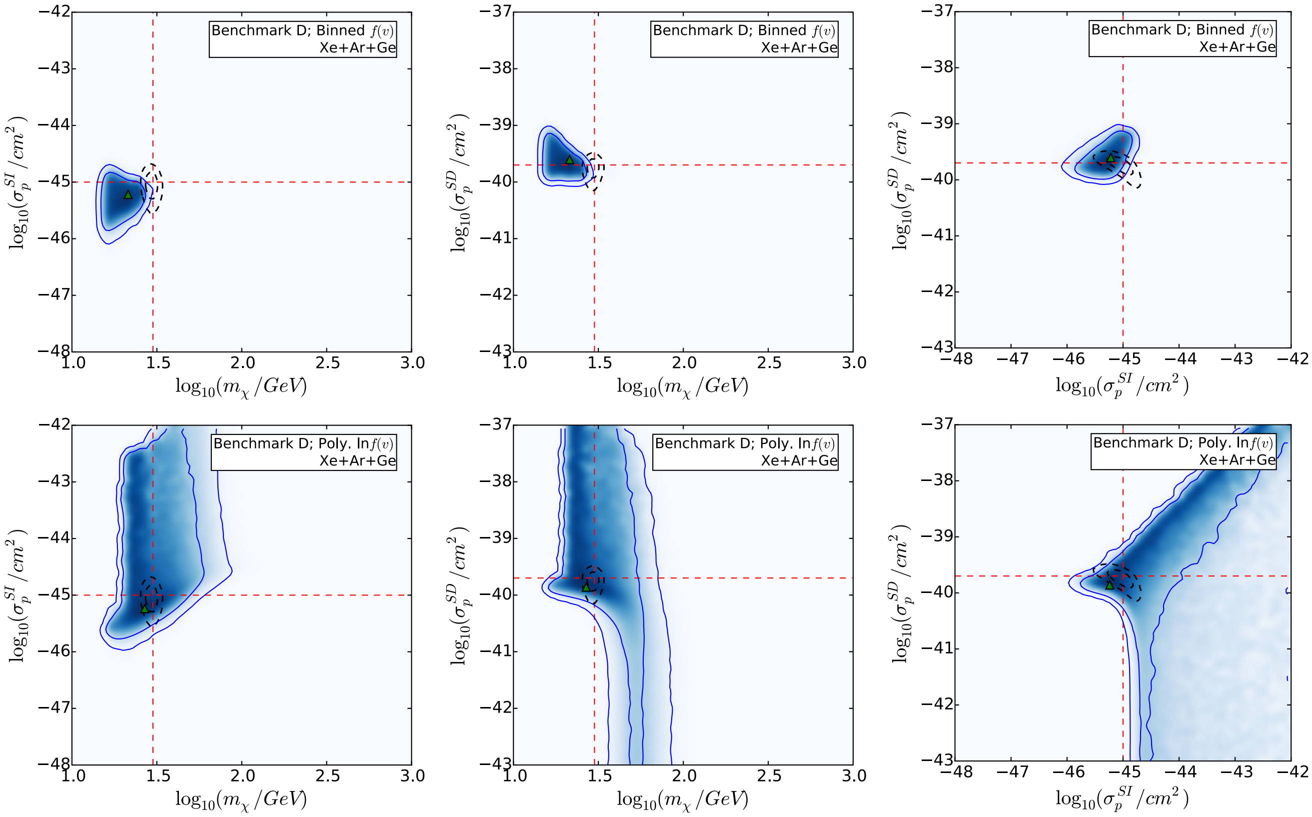

FIG. 6 (color online). Same as Fig. 2 but for benchmark D.

mass benchmarks, the fiducial spectrum is already relatively steep, requiring a velocity integral which is even steeper to give a good fit to the data at higher values of m_χ. This is possible using the rapidly-varying polynomial parametrization but not using the binned parametrization, allowing the low $\sigma_{\rm p}^{\rm SD}$ region to enter the confidence contours only in the former case.

D. Benchmark D

Finally, in Fig. 6 we show the results for benchmark D. These are very similar to those for benchmark C. This is because the contribution of the dark disk is predominantly below $v \sim 200\ \mathrm{km\,s^{-1}}$, and for a 30 GeV WIMP this is beneath the lowest speed probed by the direct detection experiments considered. The main difference with respect to benchmark C is the fact that now there is a very clear bias in the WIMP mass for the binned speed distribution. The reconstruction prefers low values of m_χ and the input parameter values are now outside the 95% contours.

In this section, we have presented the results of parameter reconstructions for $(m_\chi, \sigma_{\rm p}^{\rm SI}, \sigma_{\rm p}^{\rm SD})$ using data from multiple direct detection experiments only. As expected, when astrophysical uncertainties are neglected, the reconstruction of these parameters is very precise (apart from well-known degeneracies between the WIMP mass and cross section). When $f(v)$ is allowed to vary in the fit, the confidence contours for the parameters are significantly widened. Using the ten-bin parametrization, there is a clear bias in the WIMP mass for certain choices of benchmark parameters (in particular, benchmark D which has a light WIMP and a dark disk). This bias arises because bins of a fixed width in v correspond to smaller bins in E_R for smaller WIMP masses. This means that reducing the reconstructed WIMP mass allows a closer fit to the data, leading to the observed bias (see Ref. [31] for a detailed discussion).

The 6-polynomial parametrization does not exhibit such a bias, but leads to even larger parameter uncertainties than for the binned parametrization. Most notably, the confidence contours for the cross sections extend up to arbitrarily large values. Nonetheless, we obtain closed intervals for the WIMP mass when the input value is light (30 GeV, benchmarks C and D) relative to the mass of the detector nuclei, for both of the parametrizations of $f(v)$.

V. DIRECT DETECTION AND ICECUBE DATA

In this section, we present the results of scans performed using both direct detection and IceCube data.

A. Benchmark A

Figure 7 shows the two-dimensional profile likelihood distributions in the case of benchmark A when IceCube data are included, in addition to the three direct detection experiments. The dashed black contours now correspond to the 68% and 95% confidence contours obtained using direct detection data only for comparison. The blue contours are with IceCube data and are considerably smaller than the dashed black ones.

When astrophysical uncertainties are included, the profile likelihood is multimodal. There is a small region of allowed parameter space around the input parameter values, and a second region at large masses, large SI and negligible SD cross sections. This is true for both parametrizations, with the only slight difference being that, for the polynomial parametrization, the two regions are almost connected at the 95% confidence level. This is because the polynomial parametrization can explore a wider range of shapes for the speed distribution, allowing the data to be fit reasonably well with a wider range of WIMP masses.

The strong degeneracy in the WIMP mass, which occurs when only direct detection data are used, has been substantially reduced with the inclusion of IceCube data. Low mass WIMPs are no longer viable as they cannot produce the observed number of events above the threshold of IceCube. As discussed in Sec. IV, at large masses two scenarios were possible with direct detection data only: a region at low $\sigma_{\rm p}^{\rm SD}$, where the observed events were explained in terms of SI interactions only, and a mixed SI/SD scenario (top right corner of all the panels of Fig. 2), with velocity integrals slightly steeper than the input one of the SHM. Including the information from IceCube eliminates this second possibility, as it produces too many neutrinos in IceCube. The number of neutrinos produced in IceCube could be reduced with a $f(v)$ which goes rapidly to zero below ~200 $\mathrm{km\,s^{-1}}$. An example of such a distribution is shown in Fig. 3, labeled 'iv'. However, the shape of the resulting velocity integral cannot be reconciled with the spectrum of direct detection events, especially in the xenon experiment.

With small $\sigma_{\rm p}^{\rm SD}$ and large m_χ, good fits to the direct detection data are obtained by making the velocity integral even steeper and, since $\sigma_{\rm p}^{\rm SD}$ is small, the expected number of neutrinos is compatible with the number observed in IceCube. Therefore, the region of parameter space at large WIMP masses and small $\sigma_{\rm p}^{\rm SD}$ is still allowed when IceCube data are added.

We can again compare to the work of Arina *et al.* (in particular, the middle row of Fig. 3 of Ref. [41]). Our accurate reconstruction of the WIMP mass matches that found in Ref. [41] when direct detection and IceCube are combined. In contrast, we obtain significantly stronger constraints on the SI cross section. As previously stated, this is due to the fact that the present analysis uses an ensemble of different direct detection experiments. However, we note that here we have fully accounted for general uncertainties in the speed distribution and yet we can still obtain constraints similar to those of Arina *et al.*

B. Benchmark B

Figure 8 contains the same plots as Fig. 7, but for benchmark B, which has an additional contribution to the

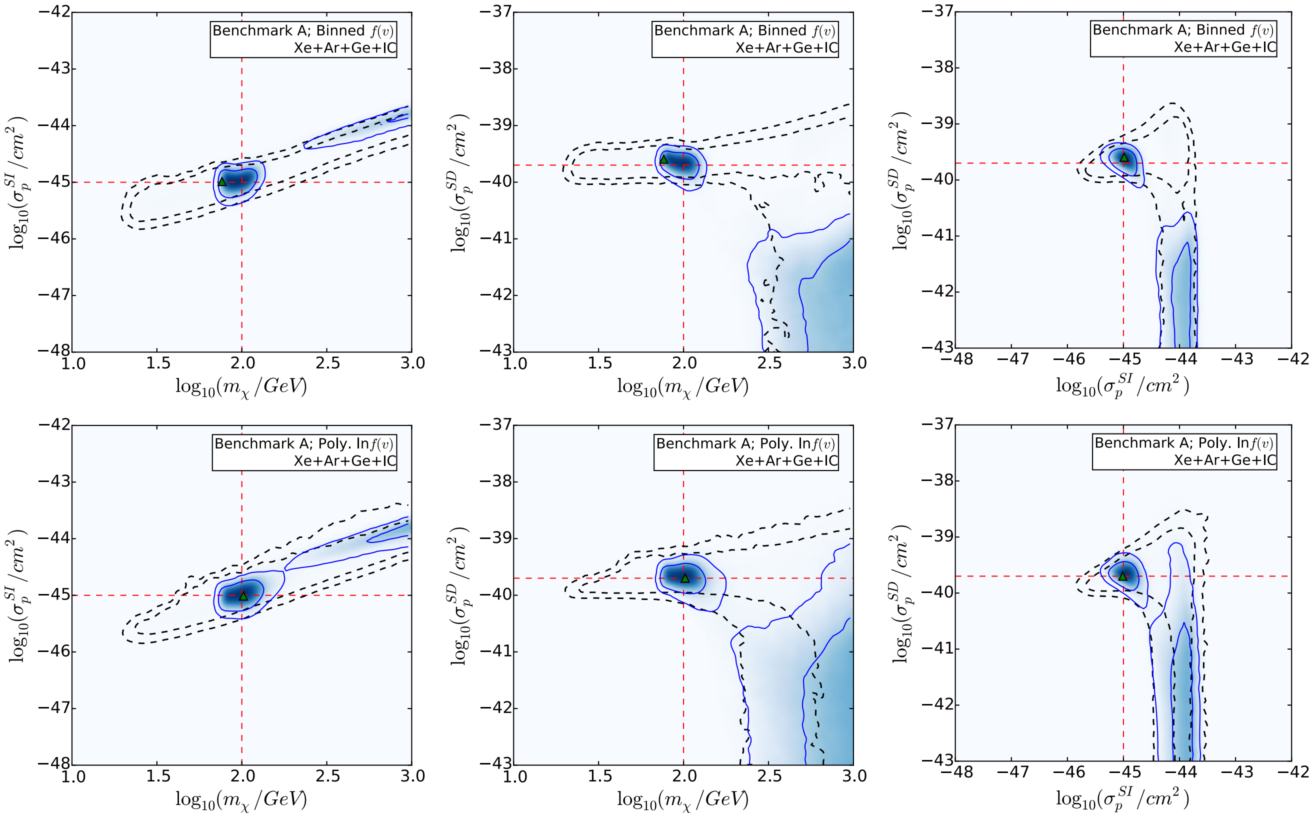

FIG. 7 (color online). Same as Fig. 2 for benchmark A but using data from both direct detection and IceCube experiments. In this case, dashed black contours show the 68% and 95% confidence contours obtained using direct detection data only (i.e., they correspond to the blue contours of Fig. 2).

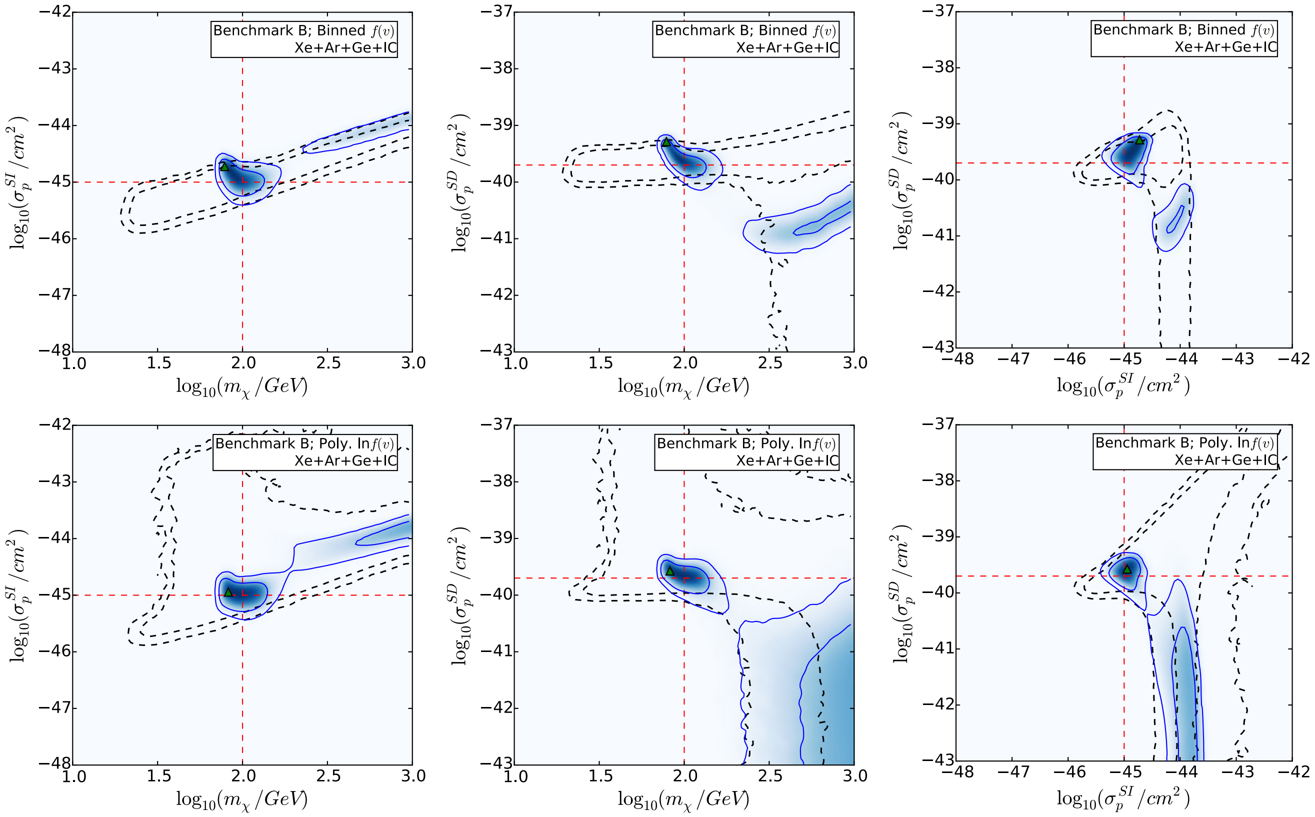

FIG. 8 (color online). Same as Fig. 7 but for benchmark B.

speed distribution from a dark disk. For both parametrizations, the results are similar to those for benchmark A. The only notable difference is that for the binned distribution (top row), the allowed region of parameter space at large masses is now bounded from below in $\sigma_{\rm p}^{\rm SD}$. In this region all the events in the direct detection experiments are due to SI interactions (and the velocity integral is quite steep) and the SD cross section is small enough not to overproduce neutrinos in IceCube. Decreasing $\sigma_{\rm p}^{\rm SD}$ further has no effect on the direct detection experiments, while underproducing the signal in IceCube. With the polynomial parametrization it is possible to compensate for this underproduction of neutrinos by increasing the speed distribution below 50–80 km $\rm s^{-1}$, where it has no effect on the direct detection experiments. However, this is not possible with the binned parametrization, since the first bin extends up to 100 km $\rm s^{-1}$ and any change would also affect the number of events in xenon. This lower bound on the SD cross section for the binned parametrization was not present for benchmark A as that benchmark only predicts 43.3 neutrinos (compared to the 242.9 of benchmark B). The smaller number of expected neutrinos means that benchmark A is less sensitive to changes in the number of neutrinos, and regions of parameter space with few neutrinos are still allowed.

Comparing the results with and without IceCube data (solid blue and dashed black contours, respectively) using the polynomial parametrization for benchmark B, we see that the regions of parameter space which extended up to large values of the cross sections are eliminated when IceCube data are included. This is most clear in the bottom right panel of Fig. 8, in which the contours no longer extend into the upper right hand corner. With direct detection data only, this region was allowed due to the possibility of having steeply rising velocity integrals for speeds which direct detection experiments could not probe. However the IceCube event rate is sensitive to these low speeds and such distributions would produce too many neutrino events.

C. Benchmark C

Figure 9 shows the same plots as Fig. 7, but for benchmark C, which has a smaller input WIMP mass. Using the binned parametrization (top row), the confidence contours are not significantly changed from the case with direct detection only. This is because the number of signal events in IceCube is just 13, which is consistent with the observed background at just over 1σ. As previously discussed, the binned distribution does not probe distribution functions which rise rapidly at low v. Because these are the only distribution functions which would be excluded by the small number of signal events, the addition of the IceCube data, therefore, has little impact on parameter reconstruction.

Using the polynomial parametrization, the region at large m_χ where both SI and SD interactions are significant is now excluded. Similarly, a part of the parameter space at high

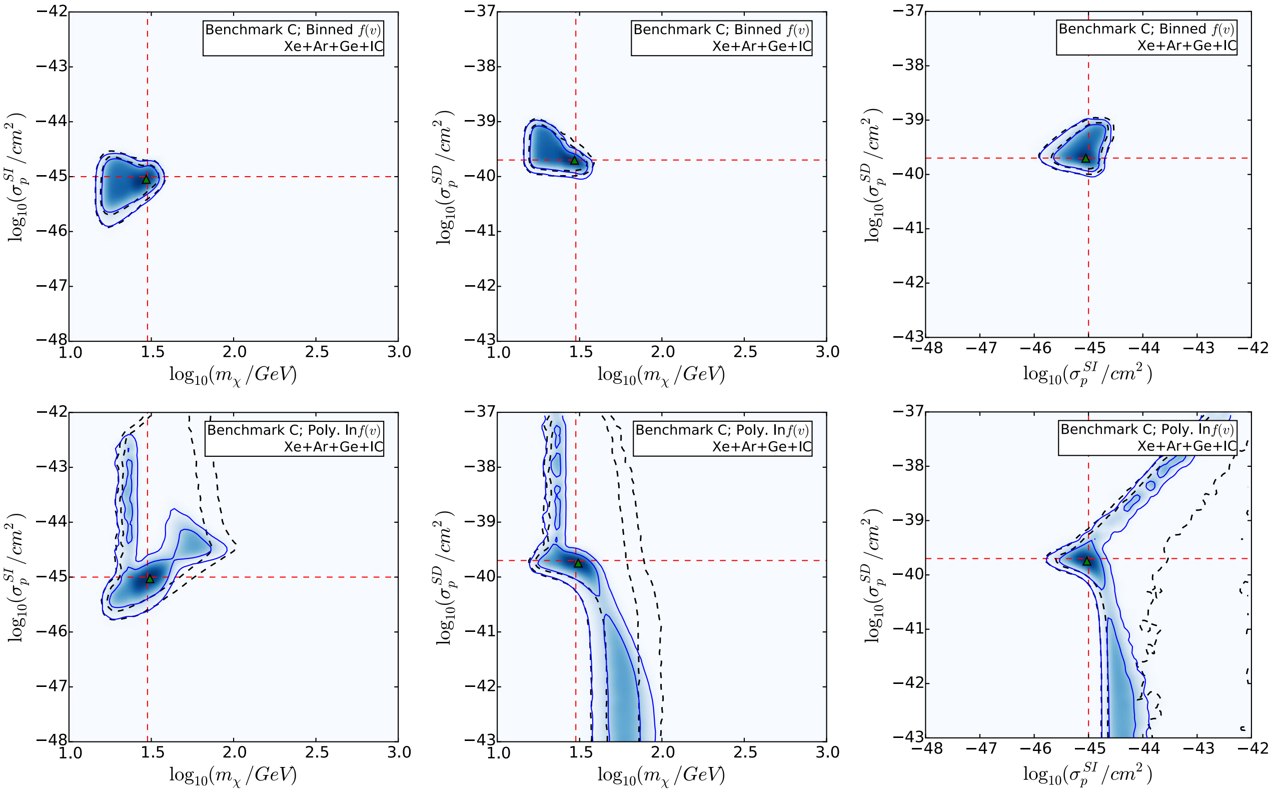

FIG. 9 (color online). Same as Fig. 7 but for benchmark C.

cross section is now also excluded. As for the higher mass benchmarks, distributions which rise rapidly at low v will overproduce events in IceCube and are, therefore, excluded. However, in contrast to the higher mass benchmarks, there remains a region which extends up to large cross sections at the 95% level. This region only occurs for WIMP masses below the sensitivity threshold of IceCube, $m_\chi = 20$ GeV. Such low-mass WIMPs produce no signal events in IceCube and, therefore, any form of $f(v)$ can fit the IceCube data set (which is consistent with background at the 1σ level).

D. Benchmark D

Figure 10 show the same plots as Fig. 9, but for benchmark D, which has a contribution from a dark disk. This results in roughly three times more IceCube events than in benchmark C, which significantly improves parameter reconstruction. For the binned parametrization, there is a noticeable shift in the contours to higher masses, so that they are more centered on the input mass value. In addition, the best-fit point lies closer to the input parameter values than in the case with only direct detection. WIMP masses below 20 GeV are excluded by IceCube data as they produce no signal events. Additionally, going to lower WIMP masses reduces the size of the bins in E_R (which was the source of the previous bias), but requires a flatter form of $f(v)$ to fit the direct detection data. This flatter distribution results in a smaller solar capture rate and is, therefore, excluded as it produces too few IceCube events. The result is that the bias towards lower WIMP masses has been eliminated by the addition of IceCube data and the benchmark values now lie within the 68% contours.

Using the polynomial parametrization, the high cross section regions of the parameter space are now entirely excluded, as the signal has a greater statistical significance than for benchmark C and cannot be explained by background alone. The shape of $f(v)$ is now reconstructed so as to neither overproduce or underproduce IceCube events. The 95% contours still extend down to small values of $\sigma_{\mathrm{p}}^{\mathrm{SD}}$. This is, as before, because the polynomial parametrization encompasses steep velocity integrals, meaning that both direct detection and IceCube data can be explained with relatively small values $\sigma_{\mathrm{p}}^{\mathrm{SD}}$. This is not the case for the binned parametrization.

In this section we have found that for model-independent parametrizations of the WIMP speed distribution, using IceCube data in addition to direct detection data significantly reduces the size of the allowed particle physics parameter space. This extends the previous results of Ref. [41] which used a fixed functional form for the speed distribution.

We find that with the addition of IceCube data, the bias in the reconstruction of the WIMP mass for the binned parametrization is substantially reduced. The best-fit parameter values now lie close to the input values for all four benchmarks. A residual degeneracy between the SI

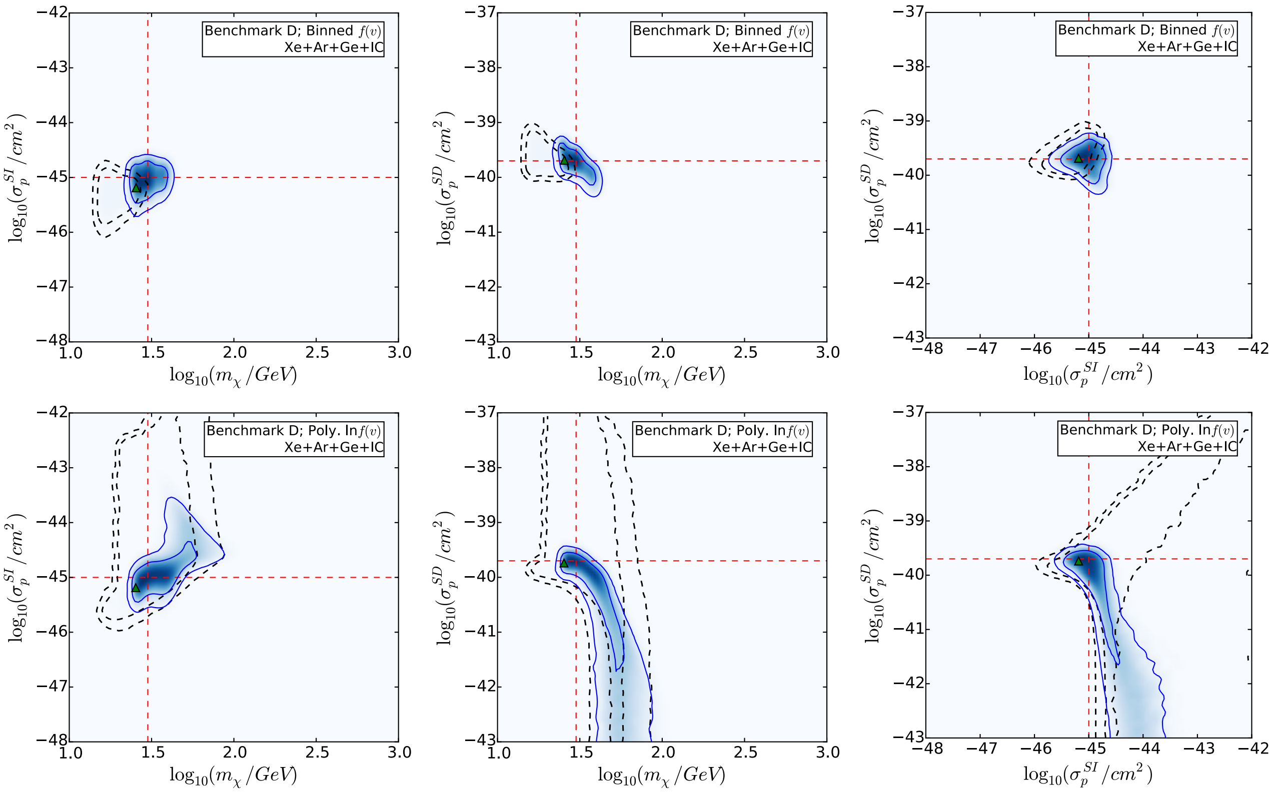

FIG. 10 (color online). Same as Fig. 7 but for benchmark D.

and SD cross sections remains and, for some benchmarks, the signals can be explained in terms of SI interactions only. However, the large cross section degeneracy which arises for the polynomial parametrization when using only direct detection data has been eliminated.

VI. RECONSTRUCTING THE SPEED DISTRIBUTION

In this section we present the reconstruction of the speed distribution using the polynomial and binned parametrizations.

A. Polynomial parametrization

In Fig. 11, we show the results for the polynomial parametrization. The solid red lines indicate the best-fit functions, while the grey bands show the 68% and 95% confidence intervals. We note that the bands are obtained for each value of v by profiling over all other values, as well as over the particle physics parameters. For reference, the SHM (dashed blue) and $\mathrm{SHM} + \mathrm{DD}$ (dot-dashed green) distribution functions used in the benchmarks are also shown. For the plots in the left column only direct detection data are used in the likelihood, while for the right column IceCube data are also used.

With only direct detection data, the uncertainties on the speed distribution are large. However, some features are apparent. For benchmark A, there is a light-grey-shaded region in the range $v \sim 200$–$400\ \mathrm{km\,s^{-1}}$ which does not lie within the 68% band. On the left side of this region, there is a contribution from flat speed distributions, such as the one labeled “i” in Fig. 3, which provide a good fit to the data for light WIMPs. On the right side of this region, there is a contribution from steeper speed distributions, such as the one labeled “ii” in Fig. 3, which provides a good fit for heavier WIMPs. Values of the speed distribution inside this light-grey region provide a poorer fit to the data as they underproduce low-energy events in xenon and/or high-energy events in argon.

This feature is not present in benchmark B because speed distributions which have low values above $v \sim 100\ \mathrm{km\,s^{-1}}$ and rise rapidly below this value are also allowed. These steeply rising distributions are those corresponding to the regions of parameter space at very large $\sigma_{\mathrm{p}}^{\mathrm{SI}}$ and $\sigma_{\mathrm{p}}^{\mathrm{SD}}$ in Fig. 4.

Similar considerations, with the speed distribution decreasing below the speeds probed by xenon and above the speeds probed by argon, also explain the behavior of the reconstruction of $f(v)$ for benchmarks C and D. However, for these benchmarks, the two regimes are closer to each other (since values of m_χ larger than 100 GeV are not allowed) and the different families of $f(v)$ overlap more.

When IceCube data are included (right panels), the constraints on $f(v)$ are significantly improved over some ranges of speed. The speed distributions which decrease below $200\ \mathrm{km\,s^{-1}}$ (as in the left panels) are eliminated, since the low m_χ values they correspond to are ruled out, as they would not produce neutrino events in IceCube. The IceCube data also disfavor the distributions which rise steeply below $v \sim 400\ \mathrm{km\,s^{-1}}$ which correspond to large values of both $\sigma_{\mathrm{p}}^{\mathrm{SI}}$ and $\sigma_{\mathrm{p}}^{\mathrm{SD}}$ (especially for benchmarks B, C and D). The net effect is that there is a range of speeds (around $200\ \mathrm{km\,s^{-1}}$ for benchmarks A and B and around $300\ \mathrm{km\,s^{-1}}$ for benchmark D) where $f(v)$ can be reconstructed within a factor of ~ 4. These speeds are just above the direct detection thresholds, where the most information about the shape of the recoil energy spectrum is available. At high speeds, $v > 600\ \mathrm{km\,s^{-1}}$, the uncertainties remain large, as the direct detection experiments have no sensitivity to the shape of $f(v)$ above E_{max}. Finally, we note that the small number of IceCube signal events in benchmark C results in only a slight improvement in the bounds on $f(v)$.

Within the range of speeds where $f(v)$ is reconstructed well, the best-fit shape for benchmarks B and D ($\mathrm{SHM} + \mathrm{DD}$) is clearly steeper than for benchmarks A and C (SHM); the reconstruction has correctly recovered the rapidly rising dark disk contribution at low speeds.

We would now like to determine whether or not it is possible to exclude any particular form for the speed distribution using the mock data. The bands in Fig. 11 are calculated from the one-dimensional profile likelihood separately at each value of v. However, the uncertainties at different values of v are strongly correlated, due to the normalization of $f(v)$. This means that not all shapes falling within the 68% band are consistent with the data at the 68% level. However, if a speed distribution falls outside the 68% band at some value of v, it can be rejected with at least 68% confidence.

A more powerful approach is to determine whether the data prefer a particular distribution over another. We focus on benchmark D, which has an input speed distribution with a dark disk and a low m_χ, which allows a more accurate reconstruction of the speed distribution as discussed above. We compare the relative log-likelihoods of the best-fit point using the polynomial parametrization with the best fit assuming a fixed SHM distribution. In order to meaningfully compare the log-likelihoods of the two best-fit points, the two scans must be performed on parameter spaces that are nested one inside the other. Therefore, we must determine the combination of Chebyshev polynomials that provides a good fit to the SHM.[4] We then fix the polynomial coefficients to the values obtained from this fit and perform a parameter scan over the remaining particle physics parameters. The best fit for the full $\ln f(v)$ parametrization has a slightly higher log-likelihood value than the best fit when the coefficients are fixed to the SHM values. The relative log-likelihood between the two models

---

[4] Decomposing $\ln f(v)$ for the SHM into six Chebyshev polynomials provides a fit which is accurate to better than 0.1%.

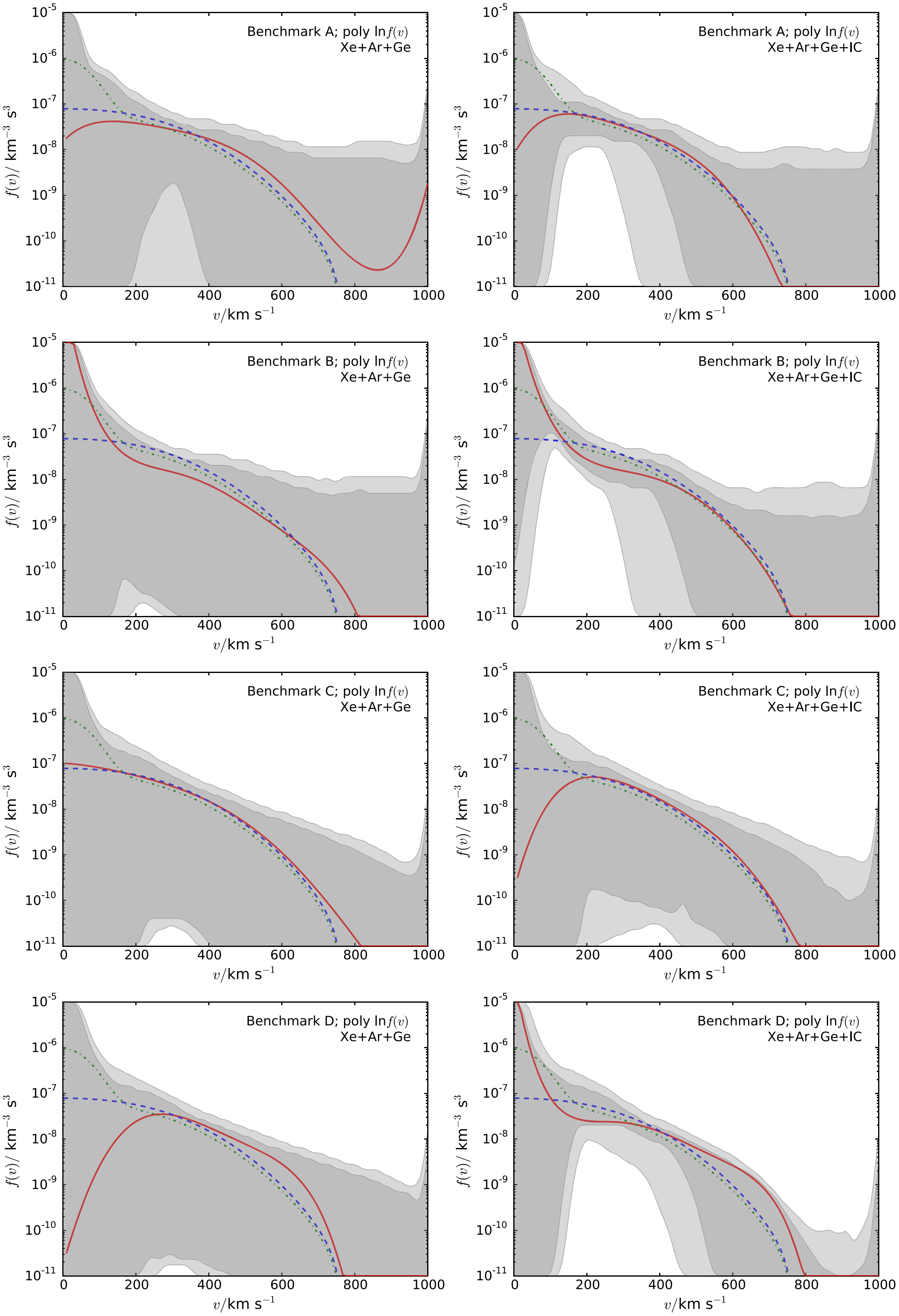

FIG. 11 (color online). Reconstructions of the speed distribution using the polynomial parametrization with six basis functions, using direct detection data only (left column) and using direct detection and IceCube data (right column). The four rows correspond to benchmarks A-D (from top to bottom). Benchmarks A and C (B and D) have the SHM (SHM + DD) as the input speed distribution. The dashed blue lines indicate the input SHM distribution while the dot-dashed green lines indicate the SHM + DD distribution. In each panel the solid red line shows the best fit, while the grey shaded bands show the 68% and 95% confidence intervals.

corresponds to a value of $\Delta\chi^2 = 2.48$. This is perhaps not surprising, as the significance of the IceCube signal is not very large ($< 3\sigma$), and it is these data which distinguish the two distributions. For 5 degrees of freedom (the 5 free polynomial coefficients in the full parametrization), the significance of this result is below the 1σ level and we, therefore, cannot reject the SHM speed distribution. However, this method allows us to make robust statements about the different speed distributions and may, with greater statistics, allow us to distinguish between them.

B. Binned parametrization

In Fig. 12, we show the speed distributions reconstructed using the binned parametrization. The red triangles show the best-fit bin heights, while the error bars indicate the 68% confidence limits. As for the polynomial parametrization, the error bar on each bin is obtained by profiling over all other parameters in the scan.

With only direct detection data, the uncertainties on the bin heights are large, with some of the 68% limits extending down to below 10^{-10} km^{-3} s^3. In certain bins, however, the constraints are much stronger, with the bin heights constrained within a factor of roughly 5. For benchmarks C and D, $f(v)$ is reconstructed with better precision for large speeds (500–700 km s^{-1}) than for the polynomial parametrization. This is because very large σ_p^{SI} and σ_p^{SD} are not allowed with the binned parametrization (see Figs. 5 and 6 and the discussion in Sec. IV). There is, however, mild tension with the input speed distribution for benchmark D (bottom left panel). In the range 500–700 km s^{-1}, the reconstruction appears to overestimate the bin heights, resulting in a flatter shape for $f(v)$ than the input form. In this case, the reconstructed WIMP mass was lower than the input value. As discussed in Ref. [31], this is because reducing the WIMP mass reduces the size of the bins when converting to energy space, which leads to a better fit to the data. When the WIMP mass is decreased, the velocity integral needs to become less steep in order to counterbalance the steepening of the spectrum. The increased WIMP population in the range 500–700 km s^{-1} is then balanced by a depleted $f(v)$ at lower speeds in order to maintain the overall normalization to unity. This results in very low bin heights in the range 100–200 km s^{-1}.

As in the case of the polynomial parametrization (Fig. 11), without IceCube data the reconstructed speed distributions for the pairs of benchmarks with and without a dark disk (A and B and C and D) are almost indistinguishable, as the direct detection experiments have little sensitivity at low speeds where they differ. When IceCube data are added, benchmarks B and D, which have a dark disk, show a clear spike in the lowest bin, which is not present for benchmarks A and C. We also note that the best-fit bin heights now trace the input speed distributions closely. As for the polynomial parametrization, the uncertainties are smallest for speeds close to the direct detection thresholds (0–300 km s^{-1} for benchmarks A and B and 200–500 km s^{-1} for the lighter benchmarks C and D).

We note that a likelihood comparison between the binned distribution and some fixed $f(v)$ such as the SHM (as was performed for the polynomial parametrization) may not be appropriate. This is because the ten-bin distribution does not provide as close an approximation to the shape of the SHM. Thus, such a likelihood comparison would not necessarily be meaningful.

VII. DISCUSSION

In Sec. IV, we examined the reconstruction of the WIMP mass and cross sections with binned and polynomial parametrizations of the speed distribution, using mock data from direct detection experiments only. As found in Refs. [4,31–33], with the binned parametrization there can be a bias in the WIMP mass. We also saw that there is a strong degeneracy between the SI and SD cross sections and the shape of the speed distribution when using only direct detection data. In particular, large cross sections can be accommodated by increasing the fraction of the WIMP population which lies below the direct detection energy thresholds. Even though this degeneracy was only apparent when using the polynomial $\ln f(v)$ parametrization, it will affect all methods which make no astrophysical assumptions. The binned parametrization of the speed distribution (top rows of Figs. 2, 4, 5 and 6) appears to lead to closed contours for the particle physics parameters. However, in the left column of Fig. 12, we demonstrate that this parametrization is insensitive to the presence of a dark disk at low speeds, and it is this lack of sensitivity that leads to the spurious upper limits on the cross sections.

With the inclusion of IceCube data in Sec. V, the situation is significantly improved. The degeneracy to large cross sections is eliminated for all four of the benchmarks that we consider. The sensitivity of solar capture to the low-speed WIMP population allows us to exclude the region of parameter space with large WIMP mass and large SI and SD cross sections, as it overproduces neutrino events at IceCube. The low mass region is also much more tightly constrained as if the mass is too small too few neutrinos are seen in IceCube. As seen in the top rows of Figs. 7, 8, and 10, the inclusion of IceCube data removes the bias in the reconstruction of the WIMP mass which occurs for the binned parametrization with direct detection data only.[5]

Some degeneracy still remains. In particular, it is possible to reduce the SD cross section significantly and compensate by increasing the SI contribution if, at the same time, the velocity integral is also made steeper at low

---

[5] In benchmarks A and B, two distinct regions of parameter space are allowed, but the one around the input parameter values is significantly preferred over the other.

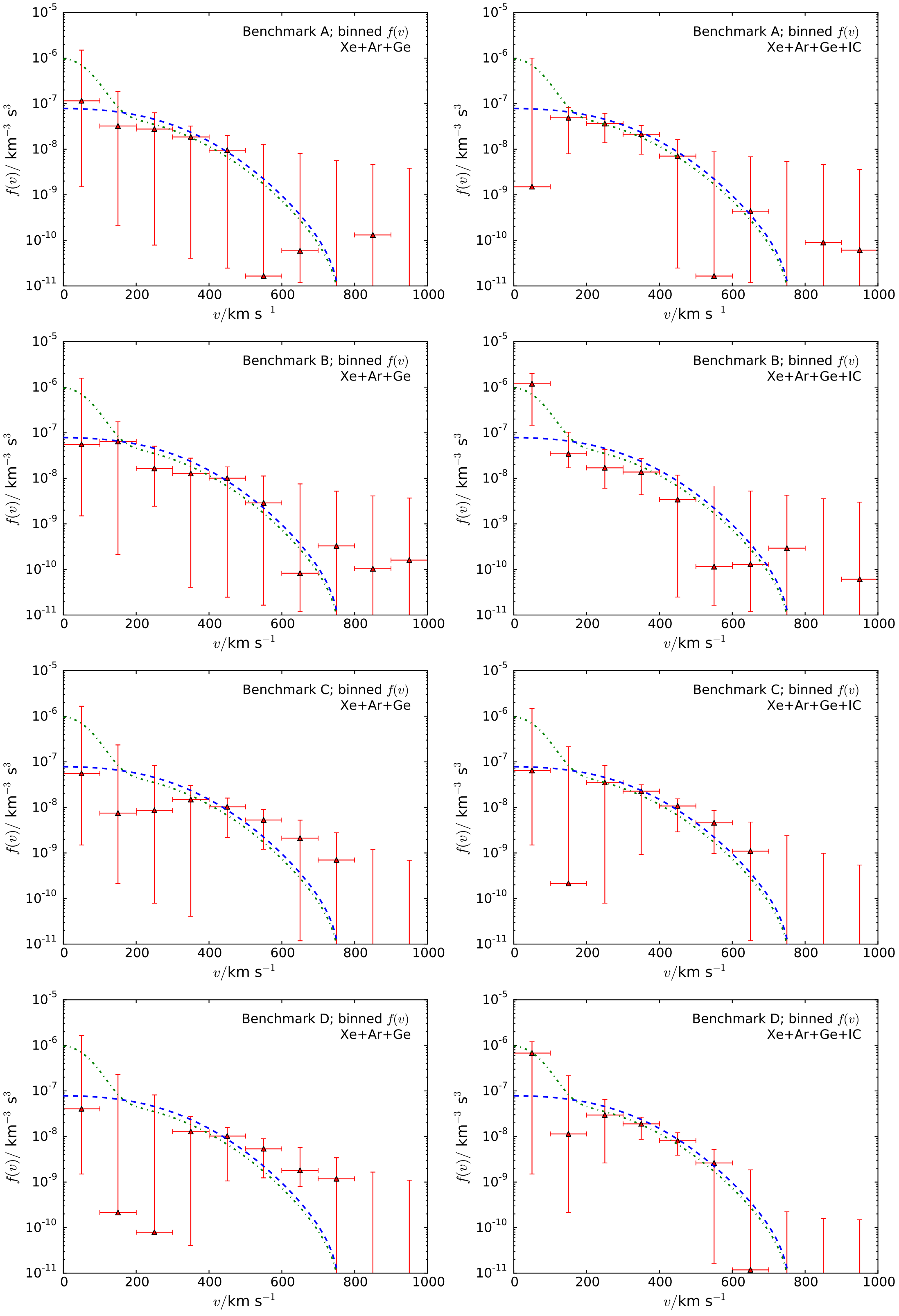

FIG. 12 (color online). Same as Fig. 11 but for the binned parametrization. The red triangles correspond to the best-fit point, while the red bars indicate the 68% confidence limits.

speeds. It is possible to define an effective cross section, $\sigma_{\rm eff}$, which incorporates both cross sections and controls the overall event rate. Due to the different response of each detector to SI and SD couplings, each experiment (including IceCube) will have a different $\sigma_{\rm eff}$. Here, for simplicity, we focus on the case of a germanium detector for which

$$\sigma_{\rm eff} = \sum_i f_i A_i^2 \sigma_{\rm p}^{\rm SI} + f_{73} \frac{16\pi}{3} \frac{\sigma_{\rm p}^{\rm SD}}{2J+1} S_{00}(0), \qquad (35)$$

where f_i and A_i are the mass fraction and mass number of isotope i. Figure 13 shows the profile likelihood for $\sigma_{\rm eff}$ with and without IceCube data (as solid and dashed lines, respectively) for benchmark D, obtained using the polynomial parametrization. Without IceCube data there is only a lower limit on $\sigma_{\rm eff}$, below which there are too few events produced in the detector. For larger values of $\sigma_{\rm eff}$, the profile likelihood is almost completely flat with an uncertainty of roughly 3 orders of magnitude. Including IceCube data, the profile likelihood becomes sharply peaked, with the value of $\sigma_{\rm eff}$ constrained to within a factor of four at the 68% level. Clearly, the inclusion of IceCube data means that we can now reconstruct the value of the effective cross section, rather than only placing a lower limit.

The residual degeneracy between the SI and SD cross sections could be broken by the inclusion of an additional direct detection experiment using a nuclear element that is sensitive mainly to SD interactions [75,76]. This approach is currently taken by the COUPP and ROSEBUD Collaborations [102,103] and is also proposed for the EURECA experiment [104].

As in Ref. [41], the conclusions we draw apply even in the absence of a significant signal at IceCube, provided the WIMP is not too light. In benchmark C, the number of signal events is just 13, which is consistent with the observed background at just over 1σ. Even with a signal of such low significance, we can still break the degeneracy between the cross section and $f(v)$, as explained above. However, if the WIMP mass is smaller than the IceCube detection threshold, no neutrino events will be produced, regardless of the scattering cross sections and speed distribution. There is, therefore, no improvement in the reconstruction of the WIMP mass and the cross section degeneracy remains.

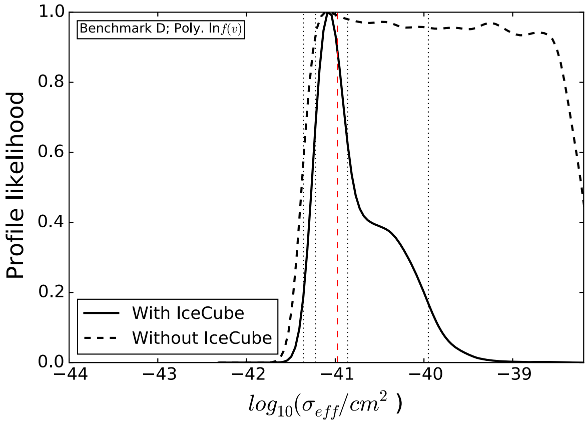

FIG. 13 (color online). Profile likelihood for the effective cross section of germanium, $\sigma_{\rm eff}$, [defined in Eq. (35)] for benchmark D, obtained using the polynomial parametrization with and without IceCube data (solid and dashed black lines, respectively). The vertical red dashed line corresponds to the input value for this benchmark while the vertical dotted black lines correspond to the 68% and 95% confidence intervals for the case *with* IceCube data.

In Sec. IV we demonstrated that the binned speed parametrization is not suitable when only direct detection data are used, as it may lead to a bias in the WIMP mass for certain benchmark parameters (see also Refs. [4,31]). With the polynomial parametrization, no such bias occurs. However, this parametrization typically results in much larger parameter uncertainties than the binned one, including a significant degeneracy to large values of the cross sections. This is due to the fact that the polynomial parametrization can explore a wider range of forms for $f(v)$, including distributions which are rapidly varying.

When IceCube data are included, the bias in the WIMP mass for the binned parametrization is significantly reduced, as low WIMP masses underproduce events in IceCube. A binned parametrization also leads to narrow parameter uncertainties (with closed contours in benchmarks B, C and D, see Figs. 8, 9 and 10) and tighter constraints on $f(v)$ than with the polynomial parametrization. This is because the reconstruction using a polynomial decomposition encompasses qualitatively different, and larger, regions of the parameter space than that using the binned $f(v)$. For example, small values of $\sigma_{\rm p}^{\rm SD}$ are allowed at the 68% level in benchmarks B, C and D, only when the polynomial parametrization is used. This is due to the fact that this parametrization can encompass steep or rapidly varying distributions which, in these regions of the parameter space, are required to produce a good fit to the data.

It is not clear which speed parametrization is optimal when direct detection and neutrino telescope data are combined. In this case, where the combined data are sensitive to the full range of WIMP speeds, the flexibility of the polynomial parametrization may not be a benefit. In particular the rapidly varying shapes it probes may not be physically well motivated. For example, it is not clear how a $f(v)$ that is rapidly varying or rising at low speeds could arise in an equilibrium model of the Milky Way. If we are confident that the speed distribution does not contain sharp features, then the binned method, which is not sensitive to such features and produces tighter constraints on the particle physics parameters, is most suitable. However, if we want to allow for a more general shape, with the possibility of sharp features, such as high density streams, the polynomial parametrization is more appropriate. A pragmatic approach would be to use both parametrizations.

We note that we have made several assumptions in this work. We have neglected uncertainties in the SD form factors, which may lead to wider uncertainties on the particle physics parameters. Using the parametrization in Ref. [56] would allow us to take this into account, and also compare the relative importance of nuclear and astrophysical uncertainties. Further simplifications include the assumptions of equilibrium between the capture and annihilation rates in the Sun, and the approximation that annihilations occur into a single channel. These uncertainties could be relaxed and incorporated as free parameters in the fit. In this paper, we focused on an idealized scenario which neglects these uncertainties in order to highlight the improvement in the determination of the WIMP particle physics and astrophysics parameters that can be achieved by combining data from a neutrino telescope with direct detection experiments. This is, however, a general phenomenon which can be exploited even for larger (and more realistic) parameter spaces.

VIII. CONCLUSIONS

We have examined the effect of combining future direct detection and neutrino telescope data on reconstructions of the standard WIMP particle physics parameters (m_χ, $\sigma_\mathrm{p}^\mathrm{SI}$ and $\sigma_\mathrm{p}^\mathrm{SD}$) and the local speed distribution $f(v)$. We account for uncertainties in the DM speed distribution by using two parametrizations: the binned parametrization proposed in Ref. [4] and the polynomial $\ln f(v)$ parametrization from Ref. [32]. Direct detection data alone are only sensitive to speeds above a (WIMP-mass-dependent) minimum value. However the inclusion of neutrino telescope data allows the full range of WIMP speeds, down to zero, to be probed.

Our main conclusions can be summarized as follows:

(i) When only data from direct detection experiments are used, the polynomial speed parametrization provides an unbiased measurement of the WIMP particle physics parameters. Even for benchmarks A and B, where the constraint contours for the particle physics parameters are not closed, the best-fit values are very close to the input values. This had previously been found for the case of SI-only interactions [32,33]. Here we have shown that it also holds when the SI and SD cross sections are both nonzero. We have also confirmed the bias in the WIMP mass induced by the binned $f(v)$ parametrization (as found in Ref. [31]).

(ii) The inclusion of IceCube mock data significantly narrows the constraints on the WIMP mass, for both the binned and polynomial parametrizations. Most notably, the bias towards lower WIMP masses experienced with the binned parametrization is removed.

(iii) For the polynomial parametrization of $f(v)$, including mock IceCube data eliminates a region of parameter space where the WIMP mass and scattering cross sections are all large. With only the data from direct detection experiments, the cross sections are degenerate with the shape of $f(v)$, so that increasing the velocity integral at low speeds (where the direct detection experiments are not sensitive), balances the effect of the large cross sections. Including the information from neutrino telescopes breaks this degeneracy, since these solutions overproduce neutrinos. The net effect is that with the addition of IceCube data, upper limits can be placed on the strength of the SI and SD cross sections.

(iv) With the combination of direct detection and neutrino data, the speed distribution is reconstructed to within an order of magnitude, over a range of speeds of $\sim$200 km s^{-1}, for all four benchmarks considered, independently of the speed parametrization employed. For the binned parametrization the accuracy achieved is better (reduced to a factor of 3–4 for certain speeds), over a range as wide as $\sim$400 km s^{-1}. The maximum sensitivity to the shape of $f(v)$ is achieved for speeds just above the threshold energies of the direct detection experiments. We have also demonstrated how these parametrizations can be used to make robust statistical comparisons between different speed distributions.

(v) Of the two parametrizations we have used, the binned method typically provides tighter constraints on both WIMP particle physics parameters and the shape of $f(v)$. The polynomial parametrization allows a broader range of speed distributions to be explored, resulting in wider uncertainties on the reconstructed parameters. Some of these speed distributions are probably not physically well motivated, for instance those that rise or fall steeply at low speeds. With data only from direct detection experiments, the polynomial parametrization should be used to avoid the bias in the WIMP mass which can arise for the binned parametrization. Given a future signal in both direct detection and neutrino telescope experiments, both parametrization methods should be used, as a consistency check. However, if the speed distribution does not contain sharp features, the binned parametrization will allow a reconstruction of the WIMP particle physics parameters, and also the speed distribution, that is reliable and more accurate.

(vi) Even with the inclusion of IceCube data, it is not always possible to derive upper and lower limits on both the SI and SD cross sections. This is due to a residual degeneracy between the two. However, it is possible to define an effective cross section, σ_eff, that determines the total event rate and incorporates both the SI and SD cross sections. The combination of direct detection and neutrino telescope data allows both upper and lower limits to be placed on σ_eff.

We have shown that by combining direct detection and neutrino telescope data, unbiased reconstructions of not only the WIMP mass, but also the WIMP interaction cross sections, can be obtained without making restrictive (and potentially unjustified) assumptions about the WIMP speed distribution. Furthermore, the form of the speed distribution can also be reconstructed. This is possible because neutrino telescopes are sensitive to the entire low-speed WIMP population that lies beneath the thresholds of direct detection experiments. The addition of neutrino telescope data, thus, solves a problem that afflicts any strategy to recover the WIMP particle physics parameters and to probe $f(v)$ using direct detection data without making astrophysical assumptions. This demonstrates, and extends, the complementarity of the different techniques employed in the search for DM.

ACKNOWLEDGMENTS

The authors thank Annika Peter and Joakim Edsjö for useful discussions. A. M. G. and B. J. K. are both supported by STFC and MF by the Leverhulme Trust. B. J. K. is also supported by the European Research Council (ERC) under the EU Seventh Framework Programme (FP7/2007-2013)/ ERC Starting Grant (Agreement No. 278234—NEWDARK project). The authors gratefully acknowledge access to the University of Nottingham High Performance Computing Facility. M. F. also acknowledges the support of project MultiDark CSD2009-00064.

---

[1] D. G. Cerdeno and A. M. Green, arXiv:1002.1912.
[2] L. E. Strigari, Phys. Rep. **531**, 1 (2013).
[3] M. W. Goodman and E. Witten, Phys. Rev. D **31**, 3059 (1985).
[4] A. H. G. Peter, Phys. Rev. D **83**, 125029 (2011).
[5] M. Feast and P. Whitelock, Mon. Not. R. Astron. Soc. **291**, 683 (1997).
[6] J. Bovy, C. A. Prieto, T. C. Beers, D. Bizyaev, L. N. da Costa *et al.*, Astrophys. J. **759**, 131 (2012).
[7] M. C. Smith, G. Ruchti, A. Helmi, R. Wyse, J. Fulbright *et al.*, Mon. Not. R. Astron. Soc. **379**, 755 (2007).
[8] T. Piffl, C. Scannapieco, J. Binney, M. Steinmetz, R.-D. Scholz *et al.*, Astron. Astrophys. **562**, A91 (2014).
[9] N. W. Evans, C. M. Carollo, and P. T. de Zeeuw, Mon. Not. R. Astron. Soc. **318**, 1131 (2000).
[10] L. M. Widrow, Astrophys. J. Suppl. Ser. **131**, 39 (2000).
[11] N. Bozorgnia, R. Catena, and T. Schwetz, J. Cosmol. Astropart. Phys. 12 (2013) 050.
[12] P. Bhattacharjee, S. Chaudhury, S. Kundu, and S. Majumdar, Phys. Rev. D **87**, 083525 (2013).
[13] M. Fornasa and A. M. Green, Phys. Rev. D **89**, 063531 (2014).
[14] M. Fairbairn and T. Schwetz, J. Cosmol. Astropart. Phys. 01 (2009) 037.
[15] M. Vogelsberger, A. Helmi, V. Springel, S. D. M. White, J. Wang, C. S. Frenk, A. Jenkins, A. Ludlow, and J. F. Navarro, Mon. Not. R. Astron. Soc. **395**, 797 (2009).
[16] M. Kuhlen, N. Weiner, J. Diemand, P. Madau, B. Moore, D. Potter, J. Stadel, and M. Zemp, J. Cosmol. Astropart. Phys. 02 (2010) 030.
[17] Y.-Y. Mao, L. E. Strigari, R. H. Wechsler, H.-Y. Wu, and O. Hahn, Astrophys. J. **764**, 35 (2013).
[18] M. Kuhlen, M. Lisanti, and D. N. Spergel, Phys. Rev. D **86**, 063505 (2012).
[19] J. I. Read, L. Mayer, A. M. Brooks, F. Governato, and G. Lake, Mon. Not. R. Astron. Soc. **397**, 44 (2009).
[20] J. I. Read, T. Bruch, L. Baudis, V. P. Debattista, O. Agertz, L. Mayer, A. M. Brooks, F. Governato, A. H. G. Peter, G. Lake, V. P. Debattista, and C. C. Popescu, AIP Conf. Proc. **1240**, 391 (2010).
[21] A. Pillepich, M. Kuhlen, J. Guedes, and P. Madau, Astrophys. J. **784**, 161 (2014).
[22] A. M. Green, Mod. Phys. Lett. A **A27**, 1230004 (2012).
[23] A. M. Green, J. Cosmol. Astropart. Phys. 10 (2010) 034.
[24] C. McCabe, Phys. Rev. D **82**, 023530 (2010).
[25] M. Drees and C.-L. Shan, J. Cosmol. Astropart. Phys. 06 (2007) 011.
[26] L. E. Strigari and R. Trotta, J. Cosmol. Astropart. Phys. 11 (2009) 019.
[27] P. J. Fox, J. Liu, and N. Weiner, Phys. Rev. D **83**, 103514 (2011).
[28] A. H. Peter, Phys. Rev. D **81**, 087301 (2010).
[29] B. Feldstein and F. Kahlhoefer, J. Cosmol. Astropart. Phys. 08 (2014) 065.
[30] A. H. Peter, V. Gluscevic, A. M. Green, B. J. Kavanagh, and S. K. Lee, Phys. Dark Univ. **5–6**, 45 (2014).
[31] B. J. Kavanagh and A. M. Green, Phys. Rev. D **86**, 065027 (2012).
[32] B. J. Kavanagh and A. M. Green, Phys. Rev. Lett. **111**, 031302 (2013).
[33] B. J. Kavanagh, Phys. Rev. D **89**, 085026 (2014).
[34] W. H. Press and D. N. Spergel, Astrophys. J. **296**, 679 (1985).
[35] J. Silk, K. Olive, and M. Srednicki, Phys. Rev. Lett. **55**, 257 (1985).
[36] T. Gaisser, G. Steigman, and S. Tilav, Phys. Rev. D **34**, 2206 (1986).
[37] L. Krauss, M. Srednicki, and F. Wilczek, Phys. Rev. D **33**, 2079 (1986).
[38] M. Srednicki, K. A. Olive, and J. Silk, Nucl. Phys. **B279**, 804 (1987).
[39] K. Griest and D. Seckel, Nucl. Phys. **B283**, 681 (1987).
[40] Webpage of the IceCube Collaboration: http://icecube.wisc.edu/.
[41] C. Arina, G. Bertone, and H. Silverwood, Phys. Rev. D **88**, 013002 (2013).

[42] G. Jungman, M. Kamionkowski, and K. Griest, Phys. Rep. **267**, 195 (1996).
[43] S. K. Lee, M. Lisanti, and B. R. Safdi, J. Cosmol. Astropart. Phys. 11 (2013) 033.
[44] C. McCabe, J. Cosmol. Astropart. Phys. 02 (2014) 027.
[45] K. Freese, J. Frieman, and A. Gould, Phys. Rev. D **37**, 3388 (1988).
[46] R. Helm, Phys. Rev. **104**, 1466 (1956).
[47] J. D. Lewin and P. F. Smith, Astropart. Phys. **6**, 87 (1996).
[48] G. Fricke, C. Bernhardt, K. Heilig, L. Schaller, L. Schellenberg, E. Shera, and C. Dejager, At. Data Nucl. Data Tables **60**, 177 (1995).
[49] G. Duda, A. Kemper, and P. Gondolo, J. Cosmol. Astropart. Phys. 04 (2007) 012.
[50] G. Co', V. De Donno, M. Anguiano, and A. M. Lallena, J. Cosmol. Astropart. Phys. 11 (2012) 010.
[51] M. Cannoni, Phys. Rev. D **84**, 095017 (2011).
[52] M. Ressell and D. Dean, Phys. Rev. C **56**, 535 (1997).
[53] J. Engel and P. Vogel, Phys. Rev. D **40**, 3132 (1989).
[54] F. Iachello, L. M. Krauss, and G. Maino, Phys. Lett. B **254**, 220 (1991).
[55] J. Ellis and R. A. Flores, Nucl. Phys. **B307**, 883 (1988).
[56] D. G. Cerdeno, M. Fornasa, J.-H. Huh, and M. Peiro, Phys. Rev. D **87**, 023512 (2013).
[57] E. Warburton, J. Becker, and B. Brown, Phys. Rev. C **41**, 1147 (1990).
[58] M. T. Ressell, M. B. Aufderheide, S. D. Bloom, K. Griest, G. J. Mathews, and D. A. Resler, Phys. Rev. D **48**, 5519 (1993).
[59] V. Dimitrov, J. Engel, and S. Pittel, Phys. Rev. D **51**, R291 (1995).
[60] J. Menéndez, D. Gazit, and A. Schwenk, Phys. Rev. D **86**, 103511 (2012).
[61] M. Cannoni, Phys. Rev. D **87**, 075014 (2013).
[62] A. Gould, Astrophys. J. **321**, 571 (1987).
[63] A. Gould, Astrophys. J. **388**, 338 (1992).
[64] XENON1T at LNGS: Proposal April 2010, http://www.bo.infn.it/xenon/docs/xe1t_proposal_v2.pdf.
[65] SuperCDMS update: http://www.fnal.gov/directorate/program-_planning/all_experimenters_meetings/special_reports/B-auer_supercdms_status_02_04_13.pdf.
[66] L. Grandi, Ph.D. thesis, University of Pavia, 2005.
[67] A. H. G. Peter, Phys. Rev. D **79**, 103532 (2009).
[68] M. Aartsen *et al.* (IceCube Collaboration), arXiv:1309.7007.
[69] M. Blennow, J. Edsjo, and T. Ohlsson, J. Cosmol. Astropart. Phys. 01 (2008) 021.
[70] P. Baratella, M. Cirelli, A. Hektor, J. Pata, M. Piibeleht, and A. Strumia, J. Cosmol. Astropart. Phys. 03 (2014) 053.
[71] P. Gondolo, J. Edsjo, P. Ullio, L. Bergstrom, M. Schelke, and E. A. Baltz, J. Cosmol. Astropart. Phys. 07 (2004) 008.
[72] P. Gondolo, J. Edsjö, P. Ullio, L. Bergström, M. Schelke, E. Baltz, T. Bringmann, and G. Duda, http://www.darksusy.org (2014).
[73] A. M. Green, J. Cosmol. Astropart. Phys. 08 (2007) 022.
[74] M. Pato, L. Baudis, G. Bertone, R. Ruiz de Austri, L. E. Strigari, and R. Trotta, Phys. Rev. D **83**, 083505 (2011).
[75] D. Cerdeno, C. Cuesta, M. Fornasa, E. Garca, C. Ginestra *et al.*, J. Cosmol. Astropart. Phys. 07 (2013) 028.
[76] D. Cerdeno, C. Cuesta, M. Fornasa, E. Garcia, C. Ginestra *et al.*, Int. J. Mod. Phys. A **29**, 1443009 (2014).
[77] G. Cowan, K. Cranmer, E. Gross, and O. Vitells, Eur. Phys. J. C **71**, 1 (2011).
[78] C. Strege, R. Trotta, G. Bertone, A. H. Peter, and P. Scott, Phys. Rev. D **86**, 023507 (2012).
[79] M. Danninger and E. Strahler, *Proc. 32nd ICRC, Beijing* 5, 141 (2011).
[80] H. Silverwood, P. Scott, M. Danninger, C. Savage, J. Edsjö, J. Adams, A. M. Brown, and K. Hultqvist, J. Cosmol. Astropart. Phys. 03 (2013) 027.
[81] P. Scott, C. Savage, J. Edsjö*et al.* (IceCube Collaboration), J. Cosmol. Astropart. Phys. 11 (2012) 057.
[82] R. Abbasi *et al.* (ICECUBE Collaboration), Phys. Rev. Lett. **102**, 201302 (2009).
[83] D. Akerib *et al.* (LUX Collaboration), Phys. Rev. Lett. **112**, 091303 (2014).
[84] E. Aprile *et al.* (XENON100 Collaboration), Phys. Rev. Lett. **111**, 021301 (2013).
[85] M. Aartsen *et al.* (IceCube collaboration), Phys. Rev. Lett. **110**, 131302 (2013).
[86] M. Cirelli, G. Corcella, A. Hektor, G. Hutsi, M. Kadastik, P. Panci, M. Raidal, F. Sala, and A. Strumia, J. Cosmol. Astropart. Phys. 03 (2011) 051.
[87] L. Roszkowski, E. M. Sessolo, and A. J. Williams, J. High Energy Phys. 02 (2015) 014.
[88] R. Schönrich, Mon. Not. R. Astron. Soc. **427**, 274 (2012).
[89] T. Bruch, J. Read, L. Baudis, and G. Lake, Astrophys. J. **696**, 920 (2009).
[90] K. Choi, C. Rott, and Y. Itow, J. Cosmol. Astropart. Phys. 05 (2014) 049.
[91] R. Catena and P. Ullio, J. Cosmol. Astropart. Phys. 08 (2010) 004.
[92] M. Weber and W. de Boer, Astron. Astrophys. **509**, A25 (2010).
[93] L. Zhang, H.-W. Rix, G. van de Ven, J. Bovy, C. Liu, and G. Zhao, Astrophys. J. **772**, 108 (2013).
[94] F. Nesti and P. Salucci, J. Cosmol. Astropart. Phys. 07 (2013) 016.
[95] J. Read, J. Phys. G **41**, 063101 (2014).
[96] A. Gould, Astrophys. J. **368**, 610 (1991).
[97] S. Sivertsson and J. Edsjo, Phys. Rev. D **85**, 123514 (2012).
[98] F. Feroz and M. P. Hobson, Mon. Not. R. Astron. Soc. **384**, 449 (2007).
[99] F. Feroz, M. P. Hobson, and M. Bridges, Mon. Not. R. Astron. Soc. **398**, 1601 (2009).
[100] F. Feroz, M. Hobson, E. Cameron, and A. Pettitt, arXiv:1306.2144.
[101] A. M. Green, J. Cosmol. Astropart. Phys. 07 (2008) 005.
[102] E. Behnke *et al.* (COUPP Collaboration), Science **319**, 933 (2008).
[103] N. Coron, J. Gironnet, P. de Marcillac, M. Martinez, T. Redon *et al.*, *Proc. Sci.*, IDM (2011) 054.
[104] H. Kraus, E. Armengaud, C. Augier, M. Bauer, N. Bechtold *et al.*, *Proc. Sci.*, IDM (2011) 109.